Applied Catalysis B: Environmental 206 (2017) 74–88

Contents lists available at ScienceDirect

Applied Catalysis B: Environmental

journal homepage: www.elsevier.com/locate/apcatb

Acidic mesostructured silica-carbon nanocomposite catalysts for biofuels and chemicals synthesis from sugars in alcoholic solutions

Ruyi Zhong[a], Feng Yu[a], Wouter Schutyser[a], Yuhe Liao[a], Filip de Clippel[a], Li Peng[b,*], Bert F. Sels[a,*]

[a] Centre for Surface Science and Catalysis, KU Leuven, Corelab, Celestijnenlaan 200F, B3001 Heverlee, Belgium
[b] State Key Laboratory of Materials-Oriented Chemical Engineering, College of Chemistry and Chemical Engineering, Nanjing Tech University, 5 Xinmofan Road, Nanjing 210009, China

ARTICLE INFO

Article history:
Received 18 December 2016
Accepted 22 December 2016
Available online 31 December 2016

Keywords:
Sulfonated mesoporous silica-carbon nanocomposites
Evaporation induced triconstituent co-assembly
Ethanolysis of fructose
Ethyl levulinate
5-ethoxymethylfurfural
Biofuels
Kinetic modeling

ABSTRACT

Sulfonated mesostructured silica-carbon nanocomposites with varying carbon content, acidic site density and porosity, obtained *via* the one-pot evaporation induced self-assembly (EISA) synthesis, were used here to convert sugars into useful chemicals and biofuel components in alcoholic solvent. The nanocomposites show a remarkable catalytic performance in ethanol, yielding up to 80%, predominantly ethyl levulinate, 5-ethoxymethylfurfural and 2-(diethoxymethyl)-5-(ethoxymethyl)furan. Fructose is the sugar substrate of choice, but the sulfonated composites are also able to convert di- and polymeric forms of fructose. Due to a lack of a glucose-to-fructose isomerization ability, the composites are unable to form the above products from the glucose resources (glucose and cellulose), ethyl glucoside being the dominant product from these feedstocks. The composite has a peculiar hierarchical pore architecture, which is stable on shelf in ambient for at least six years. While the mesoporosity facilitates entrance and fast transport (even of soluble poly-carbohydrates like inulin and cellulose polymers), the presence of microporosity is beneficial to attain fast sugar catalysis. Since the microporosity is associated with voids in the carbon phase (preferably pyrolyzed at 400 °C), composites with high carbon contents are preferred. Due to the fast transport, reactions with fructose in ethanol run in the chemical regime in the applied thermal conditions. Kinetic inspection of the reaction further clarifies the complex network of consequent and parallel reactions, demonstrating that HMF is the main precursor of humins, while the formation of EL directly from HMF should also be considered. While this observation corroborates the protective role of alcohols like ethanol, this work also concludes based on a series of reactions in different alcohols and water, that the presence of water plays a crucial role in the HMF-to-humins formation. While alcohols are known to stabilize HMF, the unprotected HMF is fairly stable in non-aqueous reaction circumstances like in *tert*-butanol solvent.

© 2016 Elsevier B.V. All rights reserved.

1. Introduction

Sustainable process development using renewable resources for fuel and chemicals production has attracted a lot of recent attention [1–9]. Biomass, as abundant and sustainable carbon source, may have the potential to at least partially replace and complement current non-renewable fossil resources [2–4,8–13]. In this context, catalytic biomass valorization for liquid transportation fuels and platform chemicals is intensively explored worldwide. Tedious catalytic disassembling of the biomass components (cellulose, hemicellulose and lignin) into useful platform molecules is challenging and several biorefinery approaches are proposed [9]. In addition to various organosolv variants, alternative processing involving a reactive extraction, such as lignin-first, were recently suggested [7,14–18]. Once refined from lignin, polysaccharides like cellulose can be hydrolyzed into their sugar monomers in presence of several catalyst types [19–25]. Upgrading of hexose into levulinic acid (LA) and 5-hydroxylmethylfurfural (HMF), the topic of this contribution, is one interesting example of valorizing biomass within future biorefineries [26–36]. The synthesis of their alkylated forms, such as ethyl levulinate (EL) and 5-ethoxymethylfurfural (EMF), is also greatly encouraged [10,35–38].

EL and EMF are both promising candidates of the next-generation biofuels to improve and replace current petroleum based fuels [35,36,38]. EL has a high octane number and high oxygen content, making it an ideal gasoline additive [35,38]. EMF has a high energy density of 30.3 MJ/L, which is comparable to standard

* Corresponding authors.
E-mail addresses: lisa.lipeng@gmail.com (L. Peng), bert.sels@biw.kuleuven.be (B.F. Sels).

http://dx.doi.org/10.1016/j.apcatb.2016.12.053
0926-3373/© 2016 Elsevier B.V. All rights reserved.

gasoline (31.1 MJ/L) and diesel (33.6 MJ/L) [39,40]. Besides potential fuel components, they are widely applied in the flavoring and fragrance industries, and serve as versatile substrates for condensation and addition reactions in organic chemistry [35,36,41,42]. Recent commercialization for instance shows the potential of EMF to produce FDCA (furanic dicarboxylic acid; for instance, Avantium), while EL can be used for levulinic acid applications (for instance, GFBiochemicals company) [41,42].

EMF can be produced by the direct etherification of HMF [40,43–50], the treatment of 5-chloromethylfurfural (CMF) with ethanol [51], or dehydrative etherification of hexoses, like fructose [39,40,43–45,52–54] and glucose [55,56]. Fructose is a preferential feedstock for the one-pot conversion to EMF as the conversion of glucose-rich carbohydrate feedstock requires a glucose-to-fructose isomerization step [55,56]. Previously, various solid-acid catalysts have been investigated for the conversion of fructose to EMF at temperatures between 70 and 140 °C in ethanol [39,40,43,44,53,54] or mixed solvents [45,52]. Tsapatsis et al. used Amberlyst 131 for the conversion of fructose in ethanol at 70 °C and obtained 93% of EMF after 24 h [39]. EL can be produced by esterification of LA [57] or ring-opening ethanolysis of HMF [47,48,58], CMF [59], or furfuryl alcohol [60]. Levulinates can also be produced by one-pot conversion of fructose [61–64], glucose [65,66], and cellulose[67] at temperatures of 120–200 °C in the presence of SO_3H-SBA-15-D [61], H-USY [66], SO_4^{2-}/TiO_2 [62], SO_4^{2-}/ZrO_2 [65], sulfonated TiO_2-ZrO_2 [64], poly(*p*-styrenesulfonic acid)-grafted carbon nanotubes [63], niobium-based phosphate [67], *etc.* The best result regarding the production of EL from fructose was reported by Chen et al., that is 86% of EL after reaction in ethanol at 120 °C for 24 h with SO_3H-functionalized carbon materials [63]. A mixture of EMF and EL is also often obtained in the conversion of fructose [44,61]. Formation of EL (as the rehydration product) increases with both increasing temperature and residence time. Riisager et al. obtained 56% of EL and 11% of HMF-ethers from fructose after 24 h reaction at 140 °C with a SO_3H functionalized SBA-15 catalyst [61]. Bell et al. reported 71% of EMF and 16% of EL after 30 h at 110 °C using Amberlyst 15 [44].

Sulfonic acid group (SO_3H) functionalized materials are the vital catalytic component of solid acid catalysts for fructose ethanolysis to EL or EMF or both. Strong acidic sulfonated ion-exchange resins, such as Amberlyst 131 [39] and Amberlyst 15 [44], show remarkably high catalytic performance for this reaction, but these commercial resins are costly and have low thermal stability due to their fragile organic framework [68,69].

As a more stable and economical counterpart to acid resins, sulfonated carbons with relatively high thermal stability have been developed [23,24,46,58,68,70–76]. These sulfonated carbonaceous based materials have been applied as catalysts for dehydration of fructose [68], ethanolysis of HMF [46,58], hydrolysis of cellulose [23,24], esterification of fatty acids [24,70–73], acetalization of polyols with aldehydes [74–76], *etc.* One facile approach to synthesize such sulfonated carbon materials is by incomplete carbonization of carbohydrates to generate polycyclic aromatic carbon sheets which are easily sulfonated by H_2SO_4 [24,72,77]. However, due to the low surface area (<2 m^2/g), SO_3H groups in such amorphous carbon bulk may not be accessed by the reactants and lead to low catalytic activity [24,77]. Creating a stable porous structure may therefore be a great solution, but only few mesoporous carbons withstand the harsh condition of sulfonation, *e.g.,* in concentrated H_2SO_4 at an elevated temperature. Since these carbons are based on mesoporous phenolic resins using either phenol or phenol derivatives like resorcinol as carbon precursors, they may not be regarded as eco-friendly [73,74].

Another strategy towards structurally ordered porous sulfonated carbon is to resort to ordered mesoporous structure of silica, forming for instance silica-carbon composite material [43,46,61,76,78,79]. Silica-carbon composites have attracted much attention in recent years, as they combine advantages of both organic and inorganic components, possessing improved structural stability and high flexibility in tuning functional groups and surface properties [80,81]. With the aid of silica structure, sulfonated carbon phases can gain better accessibility mainly in three ways [81]: i) applying a sulfur-containing organosilane precursor such as 3-mercaptopropyltrimethoxysilane in the synthesis solution of mesoporous silica [43,61,78], ii) nanocasting a sulfur-containing carbon precursor such as *p*-toluene sulfonic acid [46] or other precursors such as sucrose [71], 2,3-dihydroxynaphthalene [79], and resorcinol-formaldehyde resin [75] in a pre-formed silica template, which may require removal of the exotemplate [71,75], and iii) one-step co-assembly of silica and carbon precursors to form the mesoporous structure followed by pyrolysis [23,76,82,83], and sulfonation [23,83]. The third one-step co-assembly approach is the most cost-effective one as it avoids the use of expensive S-containing siloxane and the tedious work to synthesize the silica template beforehand. Furthermore, this approach circumvents the issues of pore blocking by carbon material or aggregation of carbon material on the external surface and allows a sufficiently high carbon content allocated in the silica framework [76,81,83]. Meanwhile, due to the silica-carbon hybrid surface, the hydrothermal stability is largely enhanced compared to pure silica mesostructures [23,84].

We recently developed an eco-friendly soft template synthesis approach for sulfonated mesostructured silica-carbon nanocomposites by the evaporation-induced self-assembly (EISA) using a tri-constituents synthesis solution composed of sucrose, tetraethylorthosilicate (TEOS) and Pluronic F127 as template, as shown schematically in Scheme S1 [23,83]. A scalable synthesis procedure of the nanocomposites using classic rotavap equipment was also proposed [85]. The SO_3H groups are easily incorporated into the incompletely carbonized carbon phase by sulfonation with concentrated H_2SO_4 without destructing the porous catalyst [23,83,86]. Herein, the mesoporous sulfonated silica-carbon nanocomposite catalyst is applied in the one-pot conversion of fructose in ethanol to produce EL, EMF or a combination of both. To the best of our knowledge, this is the first time that such a soft-templating porous silica-carbon composite is used to catalyze the tandem conversion of a biomass-based substrate. The composition and pore architecture of the composite material are very versatile, and therefore these materials are very interesting objects for catalytic research. By varying the initial ratios of TEOS to sucrose and the pyrolysis temperature, the acid site density, the acid site strength, and the porosity of the composite materials are systematically tuned, and their impact on the catalysis can be studied. A reaction network including most intermediate and end products is proposed and their kinetic profiles are well described using simple kinetics. The model may be used to uncover the most challenging steps in the complex fructose conversion mechanism, and to provide first predictions of the reaction outcome depending on the process conditions and catalyst properties. Finally, transformation of other biomass-derived substrates and use of other solvents in fructose alcoholysis are investigated and the outcome is discussed in relation to the mechanistic scheme.

2. Experimental

2.1. Synthesis of sulfonated ordered mesoporous silica-carbon nanocomposites

Mesoporous silica-carbon composites were synthesized *via* the classic evaporation-induced triconstituent co-assembly (EISA) method [23,83], wherein sucrose is used as carbon precursor, pre-

hydrolyzed tetraethylorthosilicate (TEOS) as silica precursor and Pluronic F127 as template. First, 6.4 g of F127 was dissolved in 32 g of ethanol with 0.3 g of concentrated HCl (37%) by sonication. 15.7 g of a sucrose aqueous solution (composed of 5.7 g of sucrose and 10 mL H_2O) and 8.32 g of TEOS were added in sequence to the template solution. The mixture was homogenized for 1 h through sonication, then transferred into dishes to evaporate the ethanol at 40 °C for 20 h, followed by thermal treatment at 160 °C for 24 h. The as-made product, named $Si_{50}C_{50}$, was scraped from the dishes. Composites with a different effective SiO_2/C weight ratio of 1:2 and 2:1, denoted as $Si_{33}C_{66}$ and $Si_{66}C_{33}$ respectively, were prepared *via* a similar procedure, except that the mass of sucrose was altered. The as-synthesized silica-carbon composites were pyrolyzed in a tubular furnace at 400 or 550 °C for 15 h under N_2 flow to remove the F127 template and further carbonize the sucrose. The pyrolyzed silica-carbon composites were sulfonated by suspending the solid in 20 mL concentrated sulfuric acid per gram of sample in sealed Telflon-lined autoclaves at 150 °C for 15 h. The solid was washed extensively with hot distilled water (>80 °C) until no sulfate ions were detected with $Ba(NO_3)_2$. After drying at 100 °C overnight, the final product was obtained and named Si_mC_n-T-SO_3H, with m and n representing the initial weight percentages of silica and carbon components and T representing the pyrolysis temperature in °C.

2.2. Catalysts characterization

The thermogravimetric analyses (TGA) curves were obtained on a Q500 equipment (TA Instruments, Brussels, Belgium) by heating the samples from room temperature to 800 °C at 5 °C min^{-1} under O_2. Elemental analysis for carbon atom content in the sample was carried out on a vario EL cube microanalyzer. Nitrogen sorption isotherms were measured with a Micromeritics Tristar 3000 apparatus at 77 K after degassing of the samples at 120 °C in a N_2 flow overnight. The surface area was calculated with the Brunauer–Emmett–Teller (BET) equation, pore volumes with the t-plot method and pore sizes with the Brunauer–Joyner–Halenda (BJH) method based on the adsorption branch of the isotherms. X-ray diffraction (XRD) patterns were recorded with a Seifert 3003T X-ray powder diffractometer at a step of $2\theta = 0.04°$ using Cu Kα radiation. Transmission electron microscopy (TEM) images were acquired on a JEM-2100 (HR) electron microscope operating at 200 kV. The samples for TEM were prepared by depositing an ethanolic suspension of silica-carbon composite onto holey carbon copper grids and drying.

The sulfonic acid group content was determined by acid-base titration. For this, 0.05 g of previously-dried solid was stirred in 10 mL of 2 M NaCl at room temperature for 24 h and then titrated with 1 mM NaOH solution. NH_3-TPD measurements were carried out to evaluate the acid strength. For this, the sample was first dried at 150 °C overnight in a He-flow. The adsorption of NH_3 was performed at 100 °C for 1 h, followed by purging with He at the same temperature for 2 h. The sample was heated from room temperature to 1000 °C at a rate of 10 °C min^{-1} in a He-flow of 10 mL min^{-1}. The emitted gas was detected by mass spectroscopy. Signals at the mass to charge ratio (m/e) of 16 were adopted for the comparison among these sulfonated silica-carbon nanocomposites.

2.3. Catalytic reactions

The catalytic reactions were conducted in stainless steel autoclaves at autogenous pressure. Prior to reaction, all catalysts were dehydrated at 150 °C overnight. One mmol of monosaccharide (unit), 50 mg of the catalyst, 20 mg of methyl naphthalene (internal standard) and 2.67 g of ethanol (solvent and reactant) were loaded into the reactor together with a magnetic stirring bar. The reaction time was started when the reactor was put into the heating copper block preheated to 140 °C and subjected to magnetic stirring. As soon as the desired reaction time was reached, the reactor was put into an ice bath to quench the reaction. Then, the reactor was opened and about 150 μL of sample was taken from the reaction mixture under stirring at room temperature. Sulfonated carbon catalysts prepared *via* sulfonation of pyrolyzed sucrose, a zeolite (CBV720, Si/Al = 15) and an ion-exchange resin (Nafion NR50) were tested under the same reaction conditions for comparison. Stability tests of the silica-carbon nanocomposite catalyst were carried out. Reuse of a spent catalyst was done as follows: the catalyst after 6 h of reaction was separated by filtration, rinsed with ethanol and dried at 150 °C overnight before it was used in the consecutive run. The activity of the filtrate was monitored for leaching of active acid sites.

After removal of the solid catalyst by centrifugation, the reaction solution was analyzed *via* GC-FID to acquire the yields of ethyl levulinate (EL), 5-ethoxymethylfurfural (EMF) and the diethylacetalization product, 2-(diethoxymethyl)-5-(ethoxymethyl)furan (DEMEMF). DEMEMF is generally determined in trace amounts by GC, since the reactions were performed at 140 °C [44]. However, the ratio between EMF and DEMEMF can be changed by merely changing the injection volume of the ethanolic product solution for the GC analysis, indicating an almost instantaneous equilibrium. Therefore, EMF and DEMEMF were counted together as HMF-ethers. For HPLC analysis, the reaction solution was diluted 10 times with H_2O, filtrated over a 0.45 μm filter and analyzed on a HPLC instrument (Agilent 1200 series) equipped with a refractive index detector. The HPLC analyses were carried out on both a Varian Metacarb 67C (at 85 °C with H_2O as mobile phase) and a 67H column (at 35 °C with a 5 mM H_2SO_4 aqueous solution as mobile phase). HPLC analysis was used for the quantification of fructose, difructose anhydride (DFA), levulinic acid (LA), hydroxymethylfurfural (HMF), glucose, alpha- and beta- ethyl glucopyranoside (α-EGP and β-EGP), beta-ethyl fructopyranoside (EFP), ethyl formate (EF) *etc.* in molar concentrations. As the retention times of β-EGP and EFP overlap in the chromatogram, they could not be quantified directly. An indirect method uses the thermodynamic equilibrium ratio between α-EGP and β-EGP, which is α-EGP to β-EGP equaling two, in our case. By subtracting half the area of α-EGP from the area of the β-EGP + EFP signal allows an estimate of the amount of EFP. EF is not directly measurable by GC analysis as it elutes together with the solvent peak. For its HPLC analysis, the reaction solution was analyzed in a 5 mM H_2SO_4 solution flowing phase at 35 °C, which causes the hydrolysis of EF to formic acid and ethanol. The so-obtained formic acid was quantified, confirming that EF and EL are obtained always in more or less equal molar amounts. The sensitivity factors for both GC and HPLC analyses were derived from commercial standard samples. The conversion of fructose and yields of the products were calculated on a molar base according to the reaction stoichiometry, as detailed in the supporting information.

2.4. Modeling of the reaction kinetics

A simple kinetic model was derived based on the time-evolution profiles of the concentrations of substrate, intermediates and products during fructose ethanolysis, as shown in Scheme 3. Reactions are assumed in the chemical regime as the overall observed activation energies of the catalytic fructose reaction in presence of the various catalysts are above 70 kJ/mol. Some assumptions were made to simplify the kinetic model: initial rates are assumed to be pseudo-first order with respect to the corresponding starting substrates as reactions were carried out in a large excess amount of ethanol, while weak adsorption at active sites is supposed as to be able to transform heterogeneous microkinetics into classic kinetics. As a consequence, rate constants may be interpreted with caution since adsorption equilibrium constants may be included in

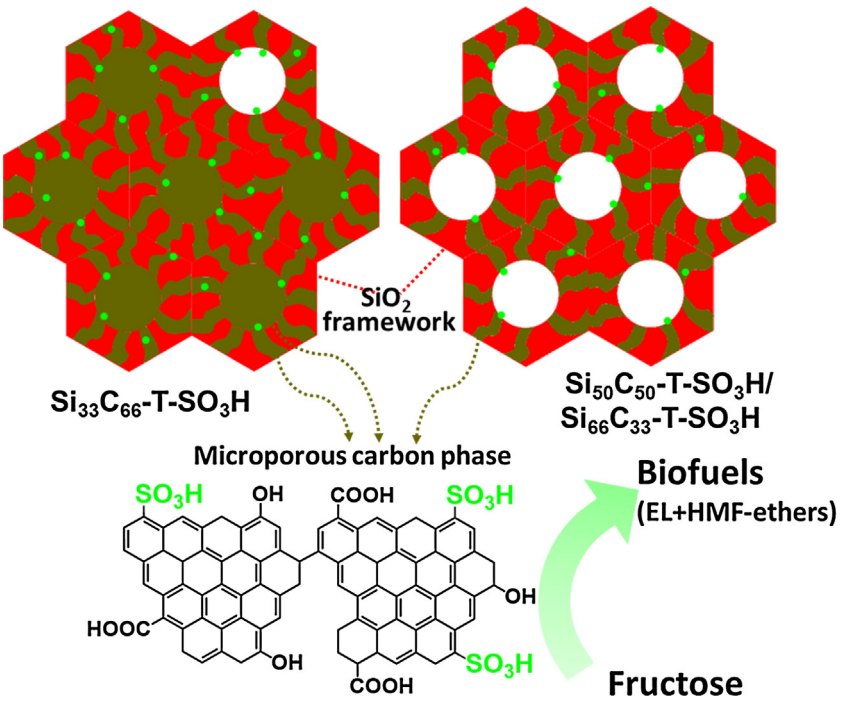

Scheme 1. Structural scheme of sulfonated silica-carbon nanocomposites. Red represents silica framework, brown represents microporous carbon phase and green represents SO_3H groups. (For interpretation of the references to colour in this figure legend, the reader is referred to the web version of this article.)

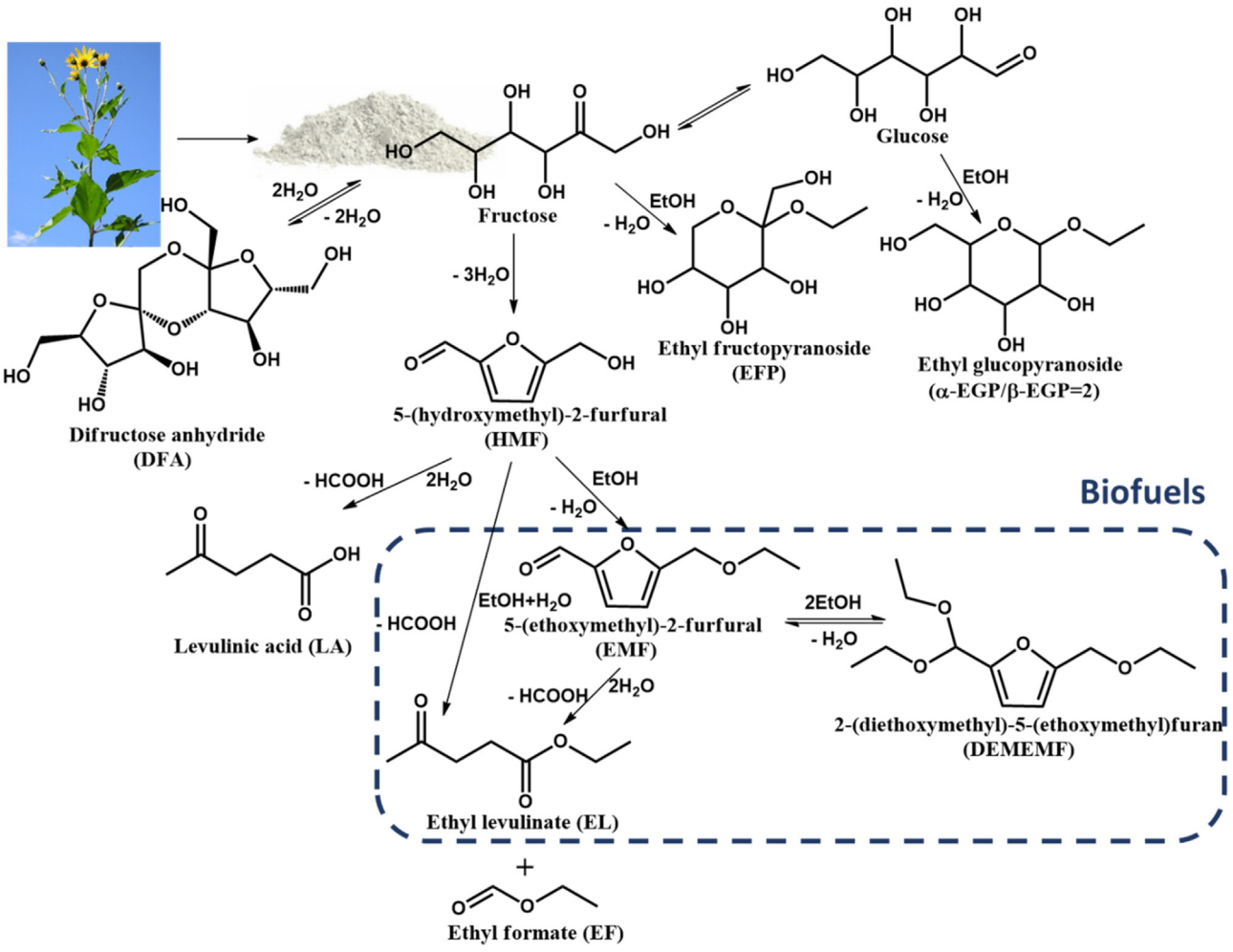

Scheme 2. Ethanolysis reaction pathway of fructose.

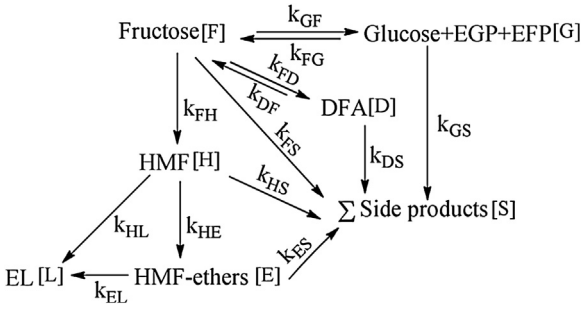

Scheme 3. A simplified kinetic model of the fructose conversion in ethanol. The side products mainly consist of humins.

the experimental rate constants. The differential equations were established according to the proposed reaction model (Scheme 3) and shown as follows:

$$\frac{d[F]}{dt} = -k_{FH}[F] - k_{FD}[F] + k_{DF}[D] - k_{FG}[F] + k_{GF}[G] - k_{FS}[F]; \quad (1)$$

$$\frac{d[H]}{dt} = k_{FH}[F] - k_{HE}[H] - k_{HL}[H] - k_{HS}[H]; \quad (2)$$

$$\frac{d[E]}{dt} = k_{HE}[H] - k_{EL}[E] - k_{ES}[E]; \quad (3)$$

$$\frac{d[L]}{dt} = k_{EL}[E] + k_{HL}[H]; \quad (4)$$

$$\frac{d[D]}{dt} = k_{FD}[F] - k_{DF}[D] - k_{DS}[D]; \quad (5)$$

$$\frac{d[G]}{dt} = k_{FG}[F] - k_{GF}[G] - k_{GS}[G]; \quad (6)$$

$$\frac{d[S]}{dt} = k_{FS}[F] + k_{HS}[H] + k_{ES}[E] + k_{DS}[D] + k_{GS}[G]. \quad (7)$$

where [F], [H], [E], [L] are the molar concentration of fructose, HMF, HMF-ethers, EL, respectively. [G] is the summed concentration of glucose, EGP and EFP; [D] is two times the molar concentration of DFA and [S] is the sum of concentrations of the side products. For the sake of simplicity, LA whose maximum selectivity is about 3% for all catalysts, was counted together with undefined humins in the pool of side products. The equations were solved to obtain the modeled time-evolution curves of the concentration using the 4th and 5th order Runge-Kutta formulas (ode45 in Matlab) with the boundary condition that $[F]|_{t=0} = 100$mol% and the initial concentration of the other species is zero. Error minimization was performed using the Matlab toolbox lsqnonlin to determine the kinetic parameters k_{FH}, k_{HE}, k_{HL}, k_{EL}, k_{FD}, k_{DF}, k_{FG}, k_{GF}, k_{FS}, k_{HS}, k_{ES}, k_{DS}, and k_{GS}, which are the experimental pseudo first order rate constants. Similar kinetic modeling has been conducted for fructose dehydration in H_2O in the presence of HCl [87] and H_2SO_4 [88], and cellulose hydrolysis in the presence of active carbon [22].

3. Results and discussion

3.1. Mesostructure and acid properties of sulfonated silica-carbon nanocomposites

The sulfonated silica-carbon nanocomposites with different carbon contents were successfully synthesized by the EISA procedure using the precursor sol, comprising of F127, TEOS and different amounts of sucrose, according to Scheme S1 [83]. During the evaporation of ethanol, the sucrose and silica oligomers associate preferentially with the polar poly(ethylene oxide) (PEO) domains of F127 micelles through hydrogen-bonding and they assemble into hexagonal mesophases. F127 is removed upon pyrolysis to generate ordered mesopores, while sucrose is incompletely carbonized.

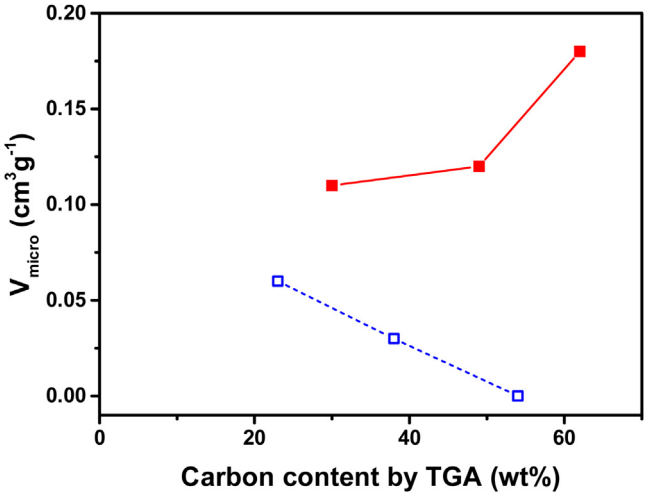

Fig. 1. Relationships between micropore volume and carbon content for Si_mC_n-400-SO_3H (■) and Si_mC_n-550-SO_3H (□).

The resulting mesoporous silica-carbon composite is sulfonated using concentrated H_2SO_4, involving electrophilic substitution of the polycyclic aromatic carbon sheets in the (hydro)carbon phases of the composites. Due to the solidified framework of silica, and unlike the mesoporous carbon structures, the mesoporous structure nicely remains unchanged after the sulfonation procedure [71,83].

The textural properties and compositions of the sulfonated silica-carbon nanocomposites are summarized in Table 1. Their TGA curves and the correlation of the carbon content (as measured by TGA) with the carbon atom content (as measured by elemental analysis) are shown in Fig. S1 and Fig. S2, respectively. Fig. S1 shows the major weight loss peak in the temperature range of 250–550 °C. This loss results from the burn-off of partially carbonized carbon phases in the composite. The comparable burn-off temperature range and linear relationship between TGA carbon content and elemental analysis carbon atom content indicate a similar degree of carbonization of the composites' carbon phase, as long as the pyrolysis step is carried out at the same temperature.

Fig. S3 shows the N_2 sorption isotherms for Si_mC_n-T-SO_3H samples. Typical IV-type N_2 sorption isotherms with a paralleled H_1-type hysteresis loop were observed for $Si_{50}C_{50}$-T-SO_3H and $Si_{66}C_{33}$-T-SO_3H, demonstrating fairly well-ordered mesoporous structures. The mesopores are generated by decomposition of the orderly arranged F127 micelles. The composites also have a considerable microporosity. As demonstrated before, this microporosity occurs mostly in the carbon but not in the silica phase [83]. Its formation is likely a consequence of the emission of gaseous decomposition products during sucrose carbonization. V_{meso} of the 400 °C pyrolysis composites decreases with increasing carbon content, while V_{micro} increases with the carbon content (Fig. 1). The mesopore volume decrease is due to a filling of the F127-generated mesopores by sucrose-derived microporous carbon. Pyrolysis at 550 °C creates both less meso- and micropore volume with increasing carbon content (Fig. 1). This is in accord with the closer stacking of the largely grown carbon sheets at the elevated pyrolysis temperature [72,77]. Increasing the pyrolysis temperature from 400 to 550 °C, diminishes V_{meso} and V_{micro}, but the decrease is less pronounced for V_{meso}, which may be explained by the resistance to shrinkage of the silica-containing pore walls [82,83].

Fig. 2 shows representative TEM images of Si_mC_n-T-SO_3H composites. In each case, mesoscopically large channels arranged in hexagonal arrays are observed. The pore sizes of *ca.* 7 nm are consistent with the value obtained from N_2 physisorption (see

Table 1
Physico-chemical properties of sulfonated silica-carbon nanocomposite catalysts and their performance in the ethanolysis reaction of fructose at 24 h.[a]

Entry	Catalyst	$[SO_3H]$[b] (mmol g^{-1})	Carbon content[c] (%)	Carbon atom content[d] (%)	S_{BET}[e] (m^2 g^{-1})	V_{meso}[f] (cm^3 g^{-1})	V_{micro}[g] (cm^3 g^{-1})	D_{pore}[h] (nm)	Yield of biofuels after 24 h[i,j] (%)
1	$Si_{33}C_{66}$-400-SO_3H	0.57 (0.92)	62	38	471	0.02	0.18	–	65 (77)
2	$Si_{50}C_{50}$-400-SO_3H	0.40 (0.81)	49	27	424	0.13	0.12	7.6	73 (44)
3	$Si_{66}C_{33}$-400-SO_3H	0.31 (1.05)	30	15	493	0.33	0.11	6.9	70 (44)
4	$Si_{33}C_{66}$-550-SO_3H	0.37 (0.68)	54	42	–	–	–	–	77 (32)
5	$Si_{50}C_{50}$-550-SO_3H	0.25 (0.66)	38	25	124	0.07	0.03	6.9	75 (30)
6	$Si_{66}C_{33}$-550-SO_3H	0.15 (0.65)	23	10	332	0.33	0.06	6.7	77 (39)
7	$Si_{66}C_{33}$-400	–	–	–	–	–	–	–	0
8	$Si_{66}C_{33}$-550	–	–	–	–	–	–	–	0
9	Sucrose-400-SO_3H	0.92	–	–	–	–	–	–	63 (58)
10	Sucrose-550-SO_3H	0.56	–	–	–	–	–	–	56 (29)
11	CBV720[k]	0.56	–	–	780	0.17	0.11	–	51 (55)
12	Nafion NR50	0.80	–	–	–	–	–	–	73 (100)

[a] Reaction conditions: fructose (180 mg), catalyst (50 mg), methyl naphthalene (20 mg) as internal standard, ethanol (2.67 g), 140 °C.
[b] Density of SO_3H groups in the silica-carbon composite was determined by titration. Values between brackets are the acid density per weight of carbon.
[c] Carbon content was determined as weight percentage of carbonaceous species in the total dry sample weight by TGA.
[d] Carbon atom content was determined by elemental analysis based on the dry sample weight.
[e] Surface area (S_{BET}) was calculated by the Brunauer–Emmett–Teller (BET) method.
[f] Mesopore volume (V_{meso}) was calculated from subtracting micropore volume (V_{micro}) from total pore volume (V_{pore}) which was obtained from the saturation plateau at high relative pressures.
[g] V_{micro} was calculated by the t-plot method.
[h] Pore size (D_{pore}) was calculated from the adsorption branch of the isotherms by the Barrett-Joyner-Halenda (BJH) method.
[i] All catalysts reached full conversion of fructose after 24 h.
[j] The molar fraction of EL in the biofuels product (EL + HMF-ethers) is indicated in the brackets.
[k] Acid sites in CBV720 were H^+.

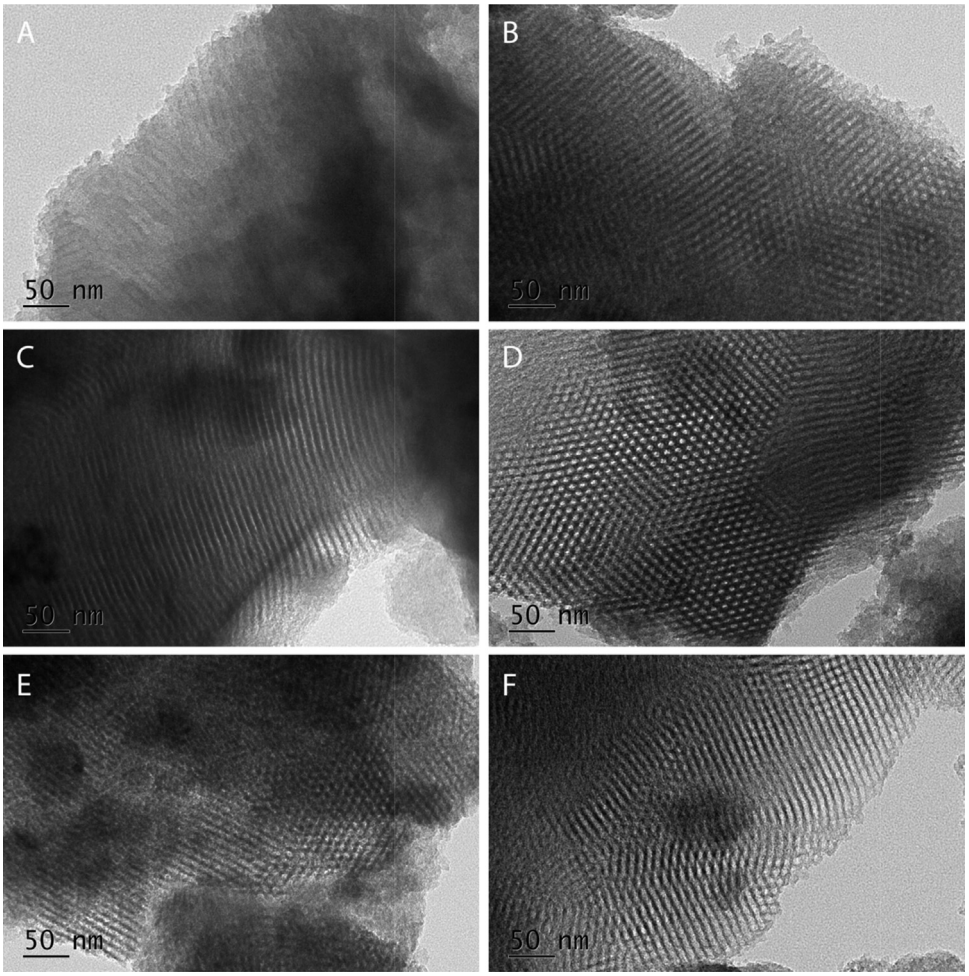

Fig. 2. TEM images of mesoporous silica-carbon nanocomposites: (A) $Si_{33}C_{66}$-400-SO_3H, (B) $Si_{33}C_{66}$-550-SO_3H, (C) $Si_{50}C_{50}$-400-SO_3H, (D) $Si_{50}C_{50}$-550-SO_3H, (E) $Si_{66}C_{33}$-400-SO_3H and (E) $Si_{66}C_{33}$-550-SO_3H.

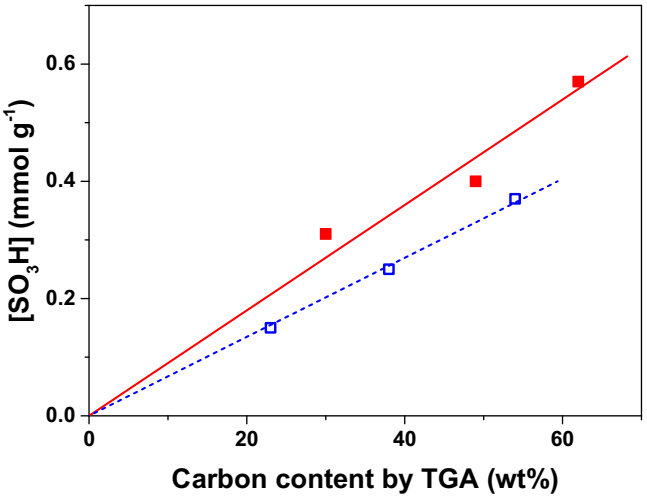

Fig. 3. Linear relationships between SO_3H site density and Carbon content for Si_mC_n-400-SO_3H (■) and Si_mC_n-550-SO_3H (□). The higher slope for the latter agrees with a lower oxygen content of the carbon phase at the higher pyrolysis temperature.

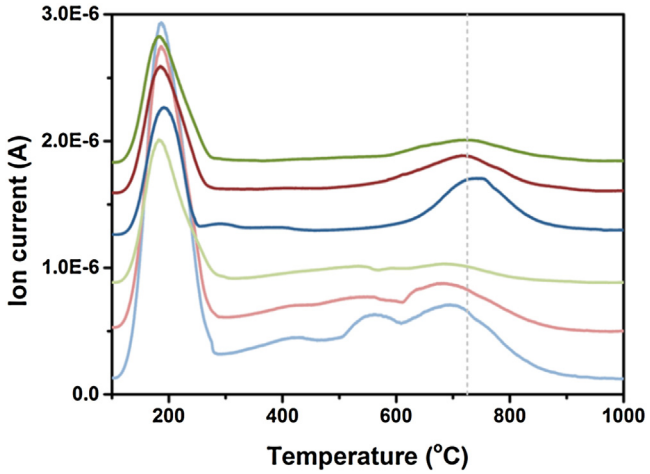

Fig. 4. NH_3 TPD profiles of $Si_{33}C_{66}$-T-SO_3H (blue), $Si_{50}C_{50}$-T-SO_3H (red), and $Si_{66}C_{33}$-T-SO_3H (green) with T equal to 400 (light) or 550 (dark) °C. (For interpretation of the references to colour in this figure legend, the reader is referred to the web version of this article.)

Fig. S3). Both $Si_{33}C_{66}$-400-SO_3H (Fig. 2A) and $Si_{33}C_{66}$-550-SO_3H (Fig. 2B), show a 2D hexagonal pattern of cylindrical channels, in line with the orderly mesostructured siliceous framework. The carbon embedded in the silica pore walls and the excessive microporous carbon in the F127-generated mesopores (for samples with high carbon content, see before) are not visible in the HRTEM images due to insufficient contrast.

Fig. S4 shows the XRD patterns of Si_mC_n-T-SO_3H. There are three low-angle diffraction peaks, which can be indexed as the (100), (110) and (200) reflections from 2D hexagonal mesostructure respectively, further evidencing therefore the ordered mesostructure of the composite materials. The diffraction at high angles shows a broad C(002) reflection at $2\theta = 16–30°$, indicative of amorphous carbon composed of polycyclic aromatic carbon sheets oriented in a rather random fashion [24,46,72,77]. There are additional weak diffraction peaks at 17°, 26° and 29°, indicating that the carbon phases in these composites may have some graphite-like carbon structures [72]. In Si_mC_n-550-SO_3H samples, an apparent C(101) diffraction peak at 45° (2θ) is also observed [77], supporting the higher carbonization degree and more structured sheet-like carbon constructs at the higher pyrolysis temperature (compare Si_mC_n-550-SO_3H and Si_mC_n-400-SO_3H). This high temperature carbon type is usually less microporous.

The carbon phases of the composite, which are polycyclic aromatic hydrocarbons from the incomplete carbonization of sucrose, can be readily sulfonated with concentrated H_2SO_4 [23,24,77,83]. The SO_3H site densities were determined by titration, as listed in Table 1. The results show that about 0.65–1.05 equivalents of acid can be created per g of carbon present in the composite, its value depending on the pyrolysis temperature. The loading of SO_3H acid sites increases almost linearly with the carbon content of the composites at each pyrolysis temperature (Fig. 3). Presence of a high carbon content in the composites is thus important to foresee sufficient number of acid sites, but the carbon content should not be too high as to avoid the obstruction of the mesopores by the excess of carbon phase. The acidity strength of these Si_mC_n-T-SO_3H samples was measured by NH_3-TPD. As seen from the TPD profiles in Fig. 4, all these sulfonated composites show two distinct major temperature peaks located at *ca.* 200 and 700 °C, corresponding to weak and strong acid sites, respectively. The low-temperature desorption peak results from silanol groups and the phenolic and carboxylic acid functionality in the incompletely carbonized sugar phases [62,65,66,68]. The high-temperature desorption peak at 400–900 °C corresponds to the strong sulfonic acid groups in the composite. The areas of these peaks are in accordance with the titration results (see Fig. 3). The peak position of desorption is shifted towards higher temperature (*ca.* 30 °C) for the samples pyrolyzed at 550 °C, when compared to those pyrolyzed at 400 °C. This shift corresponds to a higher acid strength of SO_3H groups in Si_mC_n-550-SO_3H. This can be explained by the presence of larger polycyclic aromatic carbon sheets in such composite samples [24,72,83]. Delocalization by conjugation of the negative charge of the SO_3^- groups is more pronounced in the larger carbon molecular structures, strengthening the acidity of the bound SO_3H group. This observation is in agreement with recent observations showing a higher acid strength of sulfonated polycyclic aromatic carbon from glucose pyrolysis, when compared to benzene sulfonic acid and *p*-toluene sulfonic acid [77].

To conclude, the silica-carbon composite represents a hierarchical porous material (Scheme 1), composing of an ordered mesoporous silica phase with a microporous carbon phase entangled in the silica walls. Since the mesoporosity is largely associated with the silica structure, it is less influenced by the pyrolysis temperature, though the mesopores may be partially filled with carbon in cases of the carbon-rich nanocomposites. The microporosity can be tuned with the carbon content and the pyrolysis temperature; more carbon gives higher microporosity, while low pyrolysis temperature generates structure-less carbon with micropores. Sulfonation introduces (catalytically active sulfonic) acid sites in the carbon phase; the more carbon, the higher the acid density. The strength of the acid sites can be tuned by the pyrolysis temperature; the higher the temperature, the stronger the acid site.

3.2. *On-shelf structural and catalytic stability of Si_mC_n-T-SO_3H*

The sulfonated silica-carbon solids are very stable on-shelf in ambient conditions with regard to both the pore structure and catalytic properties. As an example in Fig. 5, after six years of storage under ambient conditions, the N_2 sorption isotherms of $Si_{66}C_{33}$-400-SO_3H maintain the IV-type with a paralleled H_1-type hysteresis loop in the similar relative pressure range. The surface area (454 $m^2\,g^{-1}$), V_{meso} (0.34 $cm^3\,g^{-1}$) and V_{micro} (0.12 $cm^3\,g^{-1}$) are very close to the values of the pristine sample (Table 1, entry 6). Such extraordinary stability may result from the change of surface polarity (less hydrophilic, less susceptible to moisture) by embedding the carbon phases in the ordered silica framework. The

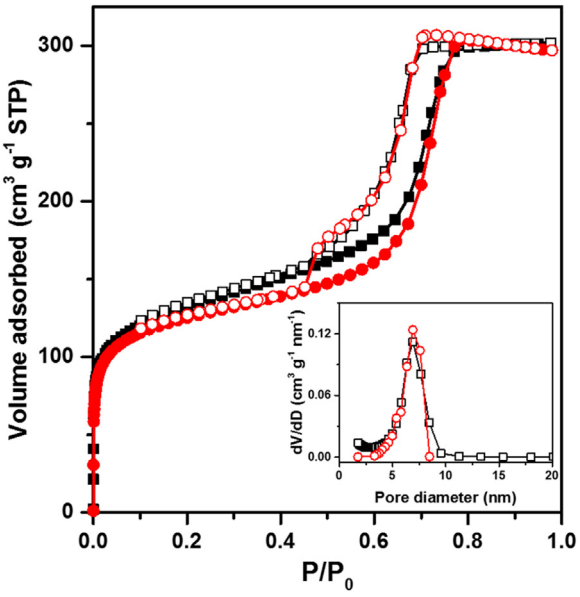

Fig. 5. N_2 sorption isotherms and pore size distributions of $Si_{66}C_{33}$-400-SO_3H before (black) and after (red) six years of storage under ambient conditions. (For interpretation of the references to colour in this figure legend, the reader is referred to the web version of this article.)

catalytic results for fructose ethanolysis on the fresh-prepared and the six-year old $Si_{66}C_{33}$-400-SO_3H samples are very close (within a difference of 10%).

3.3. *Ethanolysis of fructose to biofuels with Si_mC_n-T-SO_3H*

The series of sulfonated silica-carbon nanocomposites were first tested for the conversion of fructose in ethanol. With all catalysts, fructose was converted to the same types of products, indicating the similarity of the catalytically active sites in this set of Si_mC_n-T-SO_3H composite catalysts. The reaction pathway of fructose ethanolysis, which is proposed based on the time profile of the product distribution, is presented in Scheme 2. The scheme agrees largely with other schemes in literature [55,61,66,67]. The major difference lies in the synthesis routes of levulinate. The best fitting of our kinetic data includes two EL formation pathways (instead of the one reported) [55,61,66,67], one involving conversion of EMF, while the other route proceeds directly *via* HMF conversion.

Fig. 6 illustrates the product yields and fructose conversion in function of time in presence of the Si_mC_n-T-SO_3H composite catalysts. For all Si_mC_n-T-SO_3H, HMF and EMF are observed as the two dominant intermediates. HMF is formed *via* dehydration of fructose and EMF *via* the acid-catalyzed etherification of the alcoholic functionality of HMF. EMF is also partly converted to its diethylacetal as a consequence of the aldehyde reactivity. EMF further undergoes ring-opening rehydration to produce EL and ethyl formate (EF), according to a similar mechanism of levulinic acid formation from HMF. In parallel, EL and EF can also be formed through the direct ethanolysis of HMF by Brønsted acidity [43,49,50], passing through a common intermediate, *viz.* 2-ethoxy-5-methylidene-2,5-dihydrofuran-2-carbaldehyde [49]. EL and EF are always produced in equimolar amounts. EL is a stable end-product of the fructose ethanolysis, as there is no detectable conversion of EL under the applied reaction conditions. Considering that EMF, DEMEMF and EL are all biofuel candidates, their combined yield may be taken as the total yield of biofuels. Note that these compounds may also be considered as building blocks for bio-based polymers and building blocks [35,36,41,42].

Prior to reaching the maximum yields of HMF or HMF-ethers, difructose anhydride (DFA), which results from the dehydration of fructose [78], appeared as a major intermediate, reaching its maximum yield within 0.5 h. Therefore, it is suggested that a fast equilibrium exists between DFA and fructose, which makes DFA a reservoir of fructose. Ethyl glucopyranosides (EGP), in both α- and β-anomers and ethyl fructopyranoside in β-anomer (FGP), were detected in minor quantities (<10%). Ethyl fructofuranosides were not detected, perhaps due to the rapid isomerization to the more stable β-pyranoside isomer in presence of Brønsted acids [89]. The formation of EGP and EFP by acetalization is a competing pathway for the dehydration of fructose [56]. EGP slowly disappears with the extent of the reaction due to the shift in the acetalization equilibrium back to glucose [90], which is further converted to fructose and other products [91]. EFP also slowly isomerizes to furanosides and de-acetalizes along with the consumption of fructose in the reaction.

Based on the above time-dependent product analysis, a simplified catalytic model is proposed in Scheme 3. By modeling the experimentally obtained kinetic profiles (assuming simple pseudo first-order reactions and weak adsorption interactions at the active site), the so-obtained rate constants of the different transformations can be estimated. With these rate constants, the relative rates of all transformations over the sulfonated silica-carbon nanocomposites can be compared tentatively and perhaps interesting trends and conclusions can be draw with regard to their compositional and structural properties. The fitted kinetic profiles of the sulfonated silica-carbon nanocomposites are shown in Fig. 6.

It can be seen that the kinetic model, though simplified, very well fits the experimental results for all Si_mC_n-T-SO_3H catalysts. By taking for instance the reaction results of $Si_{33}C_{66}$-400-SO_3H in Fig. 6A as an example, a high conversion of fructose of 86% was achieved within 20 min. Meanwhile, 4% EL, 34% HMF-ethers and 22% HMF were observed together with some DFA, glucose, EGP and EFP. As the reaction progresses, HMF is consumed and the HMF-ethers yield increases to a maximum of 60% in 1.5–3 h, before they are further converted into EL. Meanwhile, EL accumulates during the reaction course, suggesting a high stability of EL under reaction conditions. After 24 h, 65% of biofuels compounds were obtained and EL comprised 77% of that product mixture (Table 1, entry 1).

Similar time evolutions of the yields of intermediates and products are observed over the other Si_mC_n-T-SO_3H catalysts (Fig. 6B–F). The yield of HMF reaches a maximum of about 30% after 0.6–3 h, while the formation of the HMF-ethers continues to increase until its maximum point or plateau is obtained after 6–10 h. This maximum yield of HMF-ethers approximates 60% with the highest experimental value of 63% in presence of $Si_{50}C_{50}$-400-SO_3H (after 6 h). The EL yield monotonically increases to 23–32% after 24 h.

The combined yield of biofuels (comprising the HMF-ethers and EL) for the different catalysts are compared in Fig. 7. All the Si_mC_n-T-SO_3H catalysts reach a total biofuel yield of 70–80% after 1.5–10 h reaction, which later in time only slightly decreases with the increased extent of EMF rehydration to EL. The percentage of EL in the biofuels after 24 h for Si_mC_n-T-SO_3H catalysts varied in the range of 30–77% (Table 1, entries 1–6), making the biofuels product suitable for further aldol condensation to long carbon fuel precursors [92]. The reaction was also carried out in presence of the non-sulfonated mesostructured silica-carbon nanocomposites to demonstrate the importance of the sulfonic acid groups. No formation of EL or HMF-ethers was detected after 24 h, only about 2% of HMF, DFA and glucose were analyzed. These results indeed confirm the necessity of the sulfonation step in the synthesis protocol and the presence of SO_3H acid sites for the effective formation of the intended biofuel from fructose.

The catalytic results of Si_mC_n-T-SO_3H catalysts were also compared with those in presence of other solid acids, like CBV720

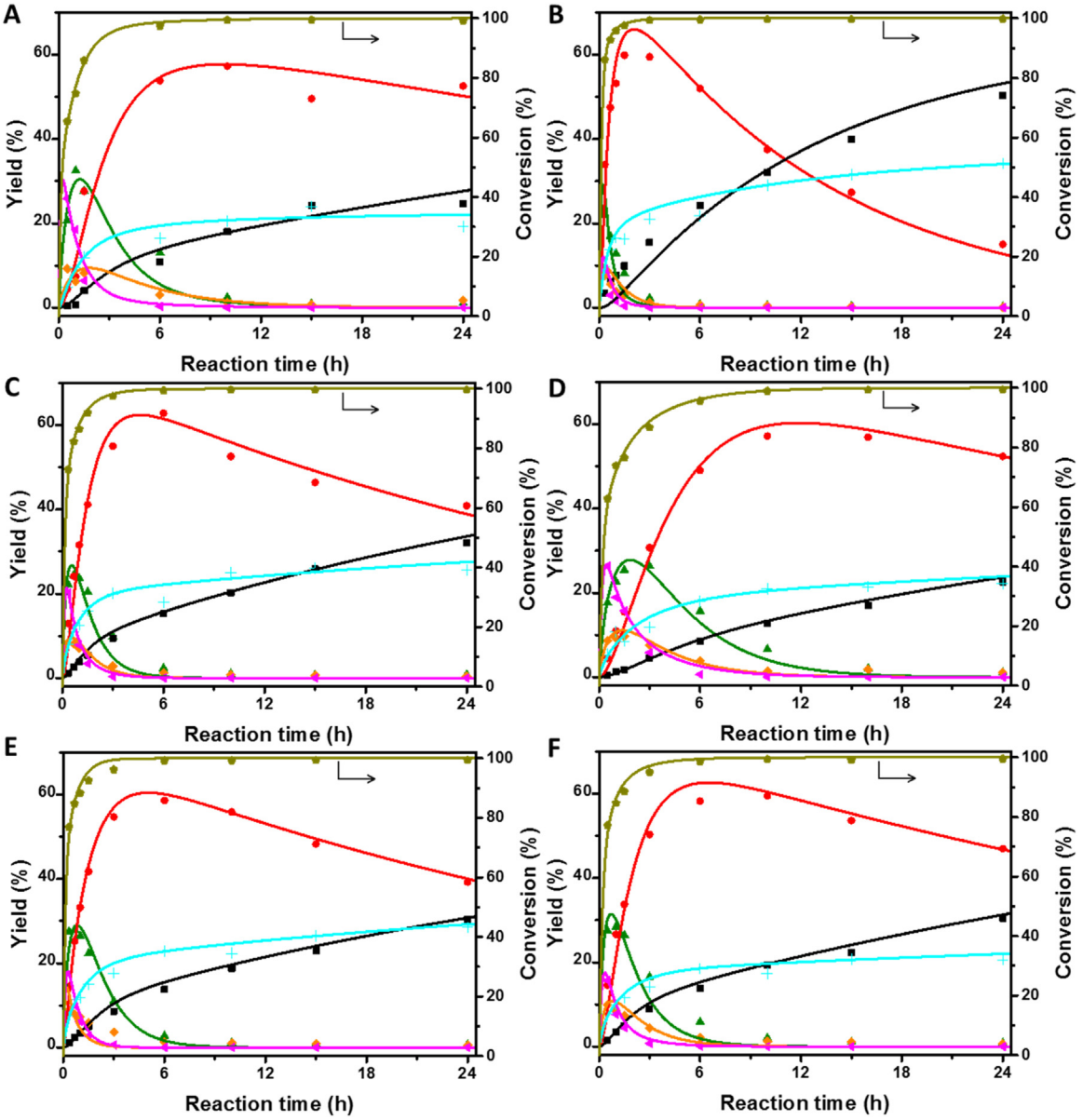

Fig. 6. Experimental and fitted kinetic profiles of ethanolysis of fructose in the presence of (A) $Si_{33}C_{66}$-400-SO_3H, (B) $Si_{33}C_{66}$-550-SO_3H, (C) $Si_{50}C_{50}$-400-SO_3H, (D) $Si_{50}C_{50}$-550-SO_3H, (E) $Si_{66}C_{33}$-400-SO_3H and (F) $Si_{66}C_{33}$-550-SO_3H. Reactant and products: fructose (⬟), EL (■), HMF-ethers (●), HMF (▲), DFA (◀), glucose + EGP + EFP (◆) and side products (+). Reaction conditions: fructose (180 mg), catalyst (50 mg), methyl naphthalene (20 mg) as internal standard, ethanol (2.67 g), 140 °C.

(Si/Al = 15), Nafion NR 50 and Sucrose-T-SO_3H, as listed in Table 1, entries 9–12. The biofuel yield over CBV720 after 24 h was only 51% (at full fructose conversion), and therefore inferior to those of the SO_3H-functionalized composite catalysts, despite its larger surface area. The poor selectivity of CBV720 might be due to the high density of strong acidic sites and narrow rigid micropores, resulting in pore blocking due the formation of intraporous humins. The sulfonated silica-carbon nanocomposites have large mesopore entrances to guarantee fast pore diffusion. Nafion NR50, a perfluorinated and sulfonated resin material with a high SO_3H site density, gave a high EL yield (73%), while less HMF-ethers are present in the reaction solution during the reaction course. This is consistent with the conclusion that very strong Brønsted acidity favors EL formation from the HMF intermediates. This result indicates that the acid sites of the silica-carbon nanocomposites may be considered less strong than those of Nafion [47]. Despite the high EL yield, Nafion is completely dissolved in the reaction medium after 24 h and cannot be separated easily from the product mixture, in contrast to the silica-carbon composites, which were easily separated after reaction. The filtrate of the reaction is free of catalytically active species, as demonstrated by the splitting test in Fig. 8C, excluding leaching of soluble aromatic sulfonates. Yet, the activity of the catalyst significantly decreased after re-use (Fig. 8C), but a slightly higher activity is obtained after re-sulfonation in concentrated H_2SO_4 for 15 h (see Fig. 8C). The higher activity is in accord with the higher content of sulfonic acid groups in the re-sulfonated sample, compared to that of the parent (0.40 *vs.* 0.31 mmol g^{-1}).

Besides the catalytic data, Fig. 8 also presents TGA and N_2 sorption results of the parent, spent and re-sulfonated catalysts. The TGA and DTG curves show a higher carbon content on the spent catalyst, mainly due to the presence of additional carbon which is removed at low temperature, *viz.* 200–350 °C. Re-sulfonation transforms these carbon deposits into more stable carbon species. This shift in carbon type was not further investigated, but is likely the result of acid-catalyzed dehydration and carbonization. The additional carbon causes a substantial loss of porosity, but the mesopore

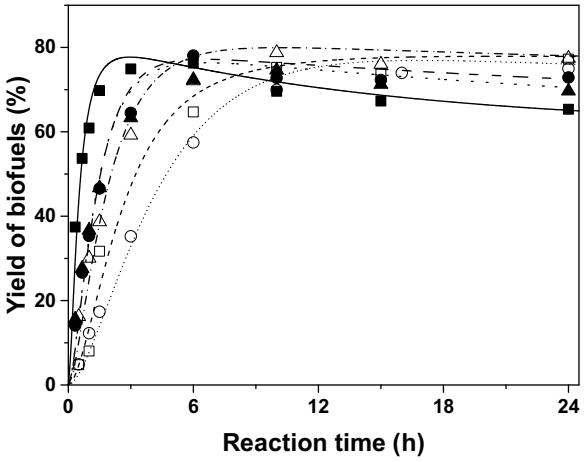

Fig. 7. Comparison of the yield of biofuels in the presence of different catalysts: $Si_{33}C_{66}$-400-SO_3H (■), $Si_{50}C_{50}$-400-SO_3H (●), $Si_{66}C_{33}$-400-SO_3H (▲), $Si_{33}C_{66}$-550-SO_3H (□), $Si_{50}C_{50}$-550-SO_3H (○) and $Si_{66}C_{33}$-550-SO_3H (△). The curves are from the fitted results to the kinetic model. Reaction conditions: fructose (180 mg), catalyst (50 mg), methyl naphthalene (20 mg) as internal standard, ethanol (2.67 g), 140 °C.

size remains largely the same. Re-sulfonation increases the microporosity, but the total porosity is slightly less than that of the parent catalyst. The characterization results reveal that the main cause of catalyst deactivation is deposition of organics (like humins) on the catalyst surface.

The high catalytic efficiency of fructose ethanolysis over sulfonated carbonaceous species may be due to the high affinity of these carbonaceous species to saccharide substrate [24,25,68,93], and the synergic effect between COOH and SO_3H groups [68]. However, the non-structured Sucrose-400-SO_3H and Sucrose-550-SO_3H, synthesized by the direct pyrolysis of sucrose and subsequent sulfonation, show considerably lower biofuel yields after 24 h, despite the presence of similar sulfonated carbon sheets and even a higher SO_3H group density [24]. These results emphasize the importance of the rigid mesoporous silica framework in the composite materials for catalysis, which is suggested to lie in two different aspects: the formation of a silica-carbon hybrid surface promotes the adsorption of carbohydrate [23], but more likely the construction of stable silica mesopores facilitates mass transport of reactants and products, whereas such transport is dramatic in the non-porous sulfonated carbon.

Table 2 displays the calculated rate constants for each step of the fructose ethanolysis cascade to EL over the Si_mC_n-T-SO_3H composite catalysts, based on the aforementioned kinetic model. Regardless of the Si_mC_n-T-SO_3H type (with varying carbon type, carbon content and number of sulfonic acid groups), the rate constant of fructose dehydration to HMF, k_{FH}, is 1.4–2.1 times k_{HE}, the rate constant of HMF etherification to EMF, and the latter is 5–10 times the rate constant of direct ethanolysis of HMF to EL, k_{HL}. In other words, the progressive reactions are always characterized with a slower rate constant. The k_{EL} values are thus the lowest, indicating that rehydration of EMF to EL is the most difficult step in the fructose to EL reaction cascade. The conversion of fructose to HMF is the fastest step for all catalysts. Though the absolute values of the rate constants k_{FH}, k_{HE}, k_{HL} and k_{EL} are different, their relative ratios are similar for the different composite catalysts. The rate constants for the interconversion between fructose and DFA are larger than those for the interconversion between fructose and EGP or between fructose and EFP, that is, $k_{FD} > k_{FG}$ and $k_{DF} > k_{GF}$. This is in accord with the multiple isomerization and acetalization steps for the latter equilibrium conversions, whereas DFA is a product of two fructose molecules and these glycosidic bonds are relatively easy to break [78]. With regard to the formation of humins, which may be considered as a loss in selectivity, a comparison of k_{ES}, k_{FS} and k_{HS} indicates that both fructose and HMF are responsible for the humins formation. Polymerization of EMF to humins is obviously hindered compared to HMF, due to the efficient protection by the alcohol into a less reactive ether group. Note that such protection is less efficient with bulky alcohols or in presence of high water contents (see below).

In order to reveal a correlation of the rate constants of Table 2 with the acidic and textural properties, k_{FH}, k_{HE}, k_{HL} and k_{EL} of the different nanocomposites were plotted against the SO_3H loading, as shown in Fig. 9. There is indeed a positive correlation for the low temperature pyrolyzed composite, while there is no significant trend for the high temperature pyrolyzed composites. The correlation with acidity indicates that most acid groups are capable of participating in the different reactions, while the acid sites of the high temperature pyrolyzed sample seem not fully accessible. These data are in agreement with the results of a recent ^{31}P NMR study, in which trimethylphosphine oxide (TMPO) was used to monitor the accessibility of the strong acid groups in similar silica-carbon nanocomposites [83]. Other correlation plots for the low pyrolyzed samples (*e.g.*, against V_{meso} and V_{micro}) were constructed after adjusting the k values to the number of acid sites (Fig. S5). Briefly, the rate constant of fructose to HMF is not influenced by the type of porosity, while the other rate constants are positively influenced by the carbon-related micropore volume and negatively by the silica-related mesopore volume. Strong acid catalyzed reactions therefore seem to occur preferably in the micropores of the carbon phase. Although not clear at the moment, the micropore confinement of the carbon and the peculiar adsorption properties therein may explain these correlations. A similar observation has been reported recently for cellulose hydrolysis on zeolite-templated microporous carbon [25].

3.4. Influence of reaction temperature

The ethanolysis of fructose was performed at different temperatures, ranging from 120 to 150 °C, in the presence of the $Si_{66}C_{33}$-550-SO_3H catalyst. The detailed experimental data and fitted kinetic curves of fructose ethanolysis on the dependence of reaction temperatures are shown in Fig. S6A-D. The kinetic model fitting matches well with the experimental results at the different temperatures. The calculated rate constants values show an acceleration of all conversion steps with the reaction temperature in agreement with Arrhenius law. Regardless of the reaction temperature, the rate constants of the four main reactions (fructose to HMF, HMF to EMF, HMF to EL and EMF to EL) follow the same activity order: $k_{FH} > k_{HE} > k_{HL} > k_{EL}$. The effect of temperature on the rate constants k_{FH}, k_{HE}, k_{HL} and k_{EL} is represented by the Arrhenius equations, as shown in Fig. 10. The apparent activation energies, $E_{a,FH}$, $E_{a,HE}$, $E_{a,HL}$ and $E_{a,EL}$ which are calculated from the slopes, are 91, 79, 80 and 71 kJ mol^{-1}, respectively. The activation energy for fructose dehydration to HMF in ethanol, $E_{a,FH}$, is lower than the value (123 kJ mol^{-1}) [88] for fructose dehydration in H_2O by H_2SO_4 (determined in a temperature window of 140–180 °C), but comparable to that in organic solvents by H_2SO_4 [94]. The apparent activation energy of HMF to EMF and HMF to EL, $E_{a,HE}$ and $E_{a,HL}$, are very close, and both lower than $E_{a,FH}$ and higher than $E_{a,EL}$. HMF formation is thus accelerated more intensively with increasing temperature than the formation of the biofuel compounds (HMF-ethers and EL), and also, the rate of HMF polymerization to humins, k_{HS}, increases more rapidly with temperature, in line with the high experimental activation energy (125 kJ mol^{-1}). Therefore, a too high reaction temperature will lower the product selectivity of the cascade process due to a preferred competitive humins pathway, despite the potential benefit of processing with a lower contact time at the higher temperature. Note that the observed

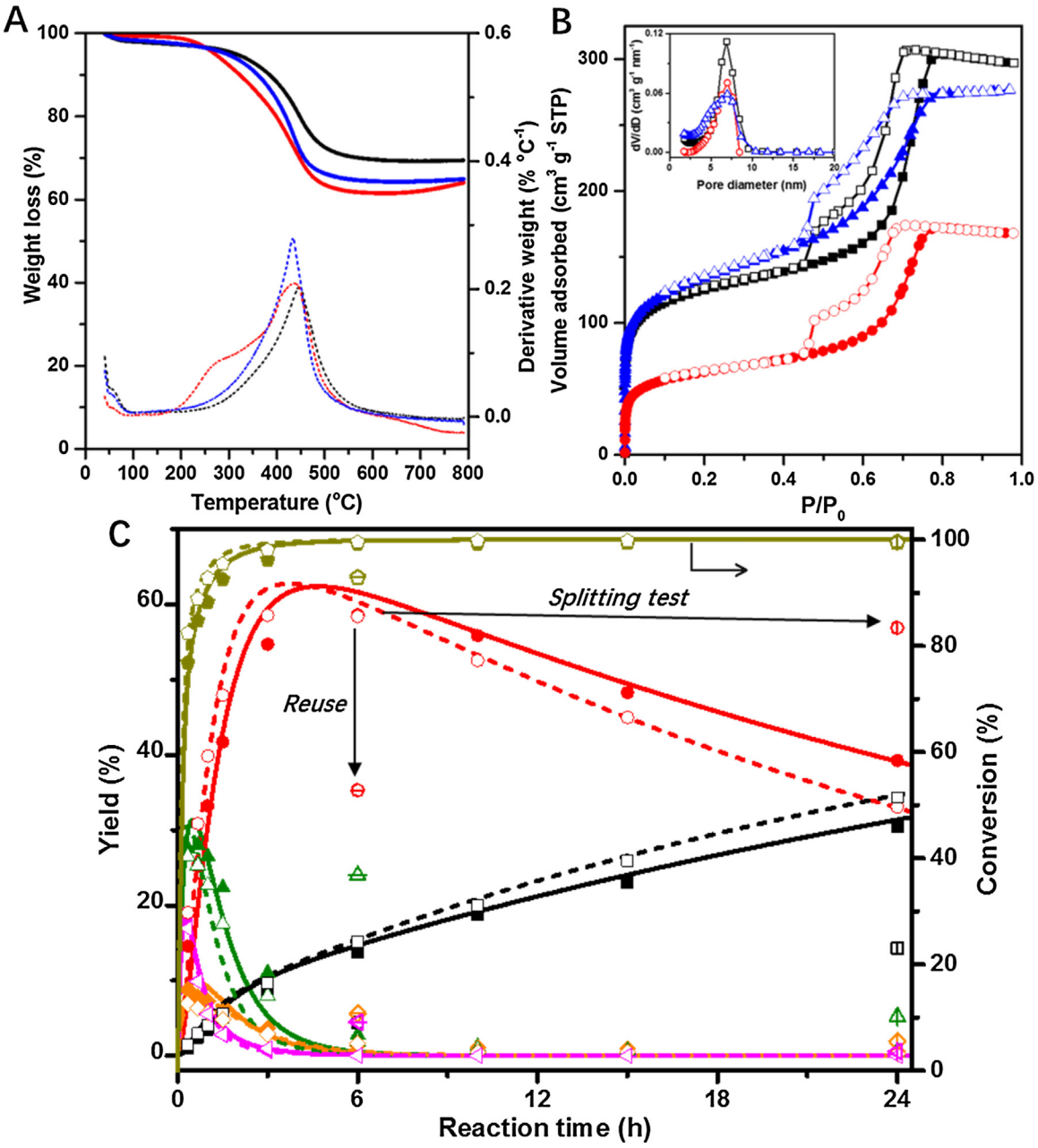

Fig. 8. (A) TGA and DTG curves, and (B) N_2 sorption isotherms and pore size distributions of the parent (black), spent (red) and re-sulfonated (blue) $Si_{66}C_{33}$-400-SO_3H catalyst. (C) Experimental and fitted kinetic profiles of fructose ethanolysis in the presence of parent (filled symbols and solid lines) and re-sulfonated (open symbols and dashed lines) catalyst. The arrow *Reuse* points to the reaction results of the spent catalyst (symbols with a horizontal bar) collected by filtration after a first 6 h run. The arrow *Splitting test* points to the reaction results of the filtrate (symbols with a vertical bar) under the same stirring and temperature conditions for another 18 h. Reactant and products: fructose (⬟), EL (■), HMF-ethers (●), HMF (▲), DFA (◀) and glucose + EGP + EFP (◆). Reaction conditions: fructose (180 mg), catalyst (50 mg), methyl naphthalene (20 mg) as internal standard, ethanol (2.67 g), 140 °C. (For interpretation of the references to colour in this figure legend, the reader is referred to the web version of this article.)

Table 2
The rate constants (h^{-1}) for each step of fructose ethanolysis over Si_mC_n-T-SO_3H catalysts.[a]

Entry	Catalyst	k_{FH}	k_{HE}	k_{HL}	k_{EL}	k_{FD}	k_{DF}	k_{FG}	k_{GF}	k_{FS}	k_{HS}	k_{ES}	k_{DS}	k_{GS}
1	$Si_{33}C_{66}$-400-SO_3H	4.57	3.26	0.39	0.05	1.92	4.39	1.07	1.89	0.48	0.41	0.02	0	0
2	$Si_{50}C_{50}$-400-SO_3H	2.00	1.31	0.19	0.02	3.02	5.23	0.7	1.47	0.42	0.06	0.01	0	0
3	$Si_{66}C_{33}$-400-SO_3H	2.39	1.16	0.15	0.02	2.45	4.31	0.65	0.99	0.39	0.11	0.01	0	0
4	$Si_{33}C_{66}$-550-SO_3H	1.09	0.53	0.11	0.01	5.09	7.66	0.25	0.32	0	0.03	0	0.36	0
5	$Si_{50}C_{50}$-550-SO_3H	0.71	0.42	0.05	0.01	2.11	3.38	0.35	0.73	0.17	0	0	0	0
6	$Si_{66}C_{33}$-550-SO_3H	1.66	0.83	0.14	0.02	1.63	3.3	0.53	0.83	0.27	0.05	0	0	0

[a] Reaction conditions: fructose (180 mg), catalyst (50 mg), methyl naphthalene (20 mg) as internal standard, ethanol (2.67 g), 140 °C.

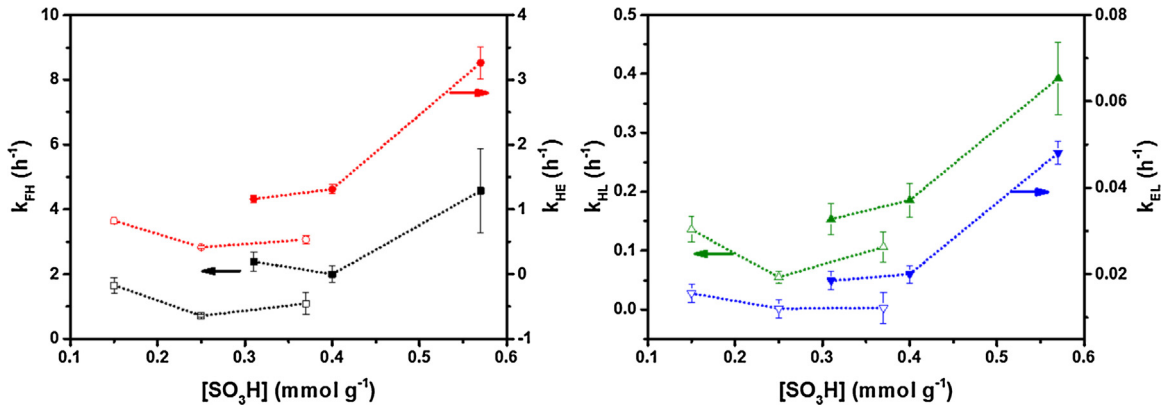

Fig. 9. Rate constants k_{FH} (■), k_{HE} (●), k_{HL} (▲) and k_{EL} (▼) with 95% confidence intervals in the ethanolysis of fructose as a function of SO_3H density of Si_mC_n-400-SO_3H (solid) and Si_mC_n-550-SO_3H (open) catalysts.

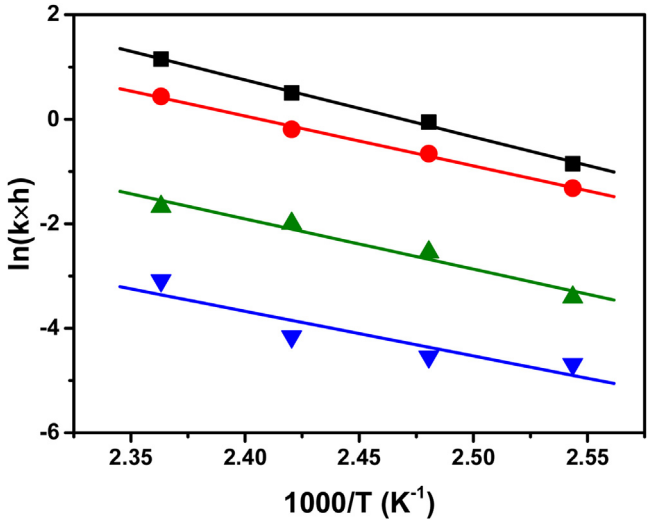

Fig. 10. Arrhenius plots of rate constants k_{FH} (■), k_{HE} (●), k_{HL} (▲) and k_{EL} (▼) for the ethanolysis of fructose in the presence of $Si_{66}C_{33}$-550-SO_3H.

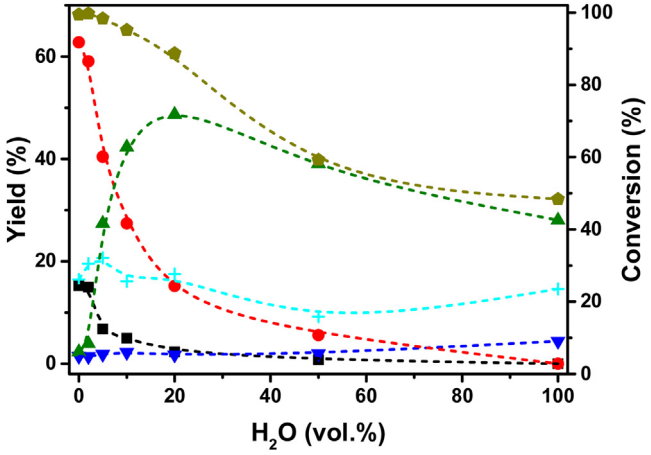

Fig. 11. Conversion and product distribution after 6 h reaction as a function of H_2O volume percentage in the ethanol-H_2O mixture solvent. Reactant and products: fructose (⬟), EL (■), HMF-ethers (●), HMF (▲), LA (▼) and humins (+). Reaction conditions: fructose (180 mg), $Si_{50}C_{50}$-400-SO_3H (50 mg), methyl naphthalene (20 mg) as internal standard, solvent (3.38 mL), 140 °C.

activation energies are all well above values that are expected for diffusion controlled reactions, and therefore merely all acid sites may be assumed to contribute to the overall conversion rate. Also note that the fastest reaction under the applied reaction conditions, *viz.* the formation of HMF from fructose, not necessarily has the lowest activation energy, as the pre-exponential factor (reaction efficiency) may be more favorable.

3.5. *Influence of the reaction solvent*

The reaction solvent may have an impact on the reaction rates and therefore on the selectivity (yield) of the catalytic cascade reaction. Reactions were therefore performed in presence of water and also in different alcoholic solvents.

The effect of H_2O content in the ethanol-H_2O solvent on the fructose conversion and the product distributions (after 6 h of reaction) is shown in Fig. 11. Water clearly retards the conversion of fructose; for instance, whereas fructose is completely converted in ethanol under the applied reaction condition, its conversion almost halved for reaction in pure water. This retardation effect may tentatively be explained by the stronger solvation effect of water (when compared to ethanol), prohibiting a fast fructose reaction at the active site, but it is more likely explained by the occurrence of different fructose tautomers in the different reaction media. It is indeed well accepted that the furanose tautomer, which occurs substantially in water-poor circumstances, more easily converts to HMF [94]. The formation of HMF increases at the expense of EMF formation up to 20 wt% of water. Higher water contents reduce the yield of HMF largely. This is not only due to the lower fructose conversion rate, but also a consequence of more pronounced humins formation. Indeed, inspection of the humins selectivity points to an increase with increasing water content. The EL yield decreases with increasing water content, but there is no significant increase of the levulinic acid yield. Irrespective of the levulinic acid synthesis route (from EL or from HMF), a competing HMF to humins conversion is responsible for the lower levulinic acid yield. These observations strongly corroborate the protective role of ethanol by etherification (and acetalization) of HMF into the more stable EMF (and DEMEMF), in agreement with literature [95].

The effect of other alcohols of different carbon chain length on the product selectivity of the fructose conversion in presence of the Si_mC_n-T-SO_3H catalysts was also studied. The conversion of fructose and the product distributions after 6 and 24 h reaction using different alkyl alcohols in the presence of $Si_{50}C_{50}$-400-SO_3H are shown in Fig. 12. The product distributions indicate that the fructose conversion proceeds similarly in these solvents (Scheme 2), with HMF and the corresponding 5-alkoxymethylfurfural being the two major intermediates and the corresponding alkyl levulinate as the final product. Note that these alkoxymethylfurfurals and lev-

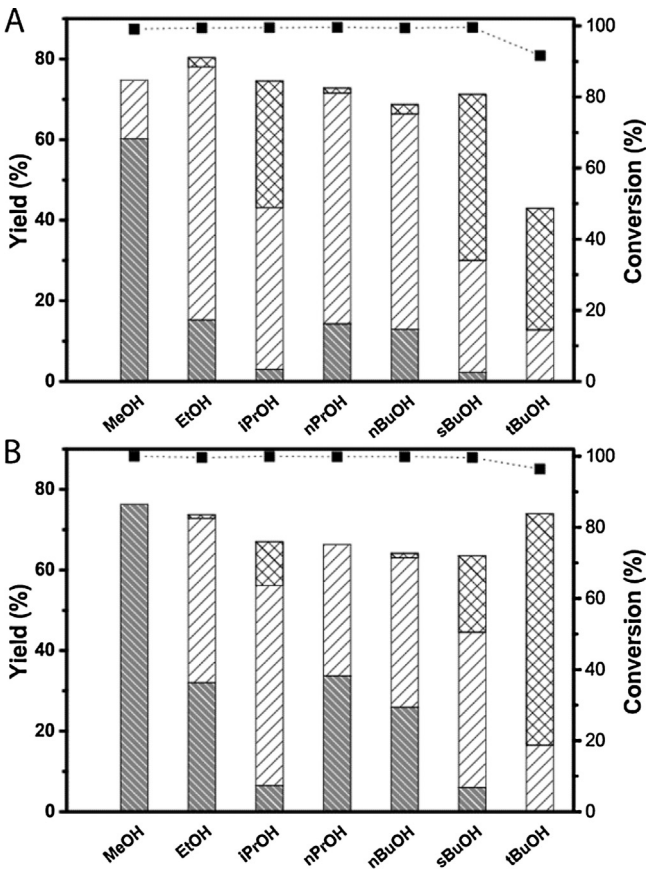

Fig. 12. Conversion of fructose (■) and yields of alkyl levulinate ( ), 5-alkoxymethylfurfural ( ) and HMF ( ) of alcoholysis of fructose in different alcohols for the reaction time of (A) 6 h and (B) 24 h. Reaction conditions: fructose (180 mg), $Si_{50}C_{50}$-400-SO_3H (50 mg), methyl naphthalene (20 mg) as internal standard, alcohol (3.38 mL), 140 °C.

ulinate esters all belong to the diesel-range biofuels, and may have future potential there [44].

Except for the bulky *tert*-butanol, complete conversion of fructose is reached within 6 h. In methanol, 60% of methyl levulinate is produced after 6 h, and after 24 h, the yield reaches 76%, which is among the highest yields reported for a one-pot conversion of fructose [63,64,66,95]. Reactions in the other linear alcohols, *viz.* ethanol, *n*-propanol and *n*-butanol, yield similar product distributions after 6 and 24 h. This indicates that the rates of the fructose conversion cascade are similar in these solvents. For the linear alcohols with alkyl chains of more than one carbons, the rates therefore do not depend on the alcohol alkyl chain length. In ethanol, *n*-propanol and *n*-butanol, the alkyl levulinates are not as easily formed as in methanol. In contrast, 54–63% of the corresponding alkoxymethylfurfural yields were obtained after 6 h with only a little HMF left. Only at longer reaction times, the alkyl levulinates are formed, with yields ranging from 26 to 33%. Chen et al. also applied ethanol, *n*-propanol and *n*-butanol for the conversion of fructose with CNT-PSSA and obtained comparably high yields of the corresponding alkyl levulinate [63]. The use of branched alcohols like *iso*-propanol, *sec*-butanol and *tert*-butanol largely delays the reaction progress. Indeed, considerable amounts of HMF are present after 6 h of reaction. After 24 h, the amount of HMF decreases at the expense of alkoxymethylfurfural formation, in the following order in agreement with the dependence of the etherification rate with increasing steric hindrance of the aliphatic chain: *iso*-propanol > *sec*-butanol > *tert*-butanol. The alkyl levulinate yield is low for all steric alcohols: in *iso*-propanol and *sec*-butanol, the yield is 3% and 7% after 6 h and 24 h, respectively, while *tert*-butyl levulinate is not observed. The dominant product after 24 h in *tert*-butanol is HMF, showing a yield of 65%. Note that this HMF yield is considerably higher than the 30% in pure water (see Fig. 11). To conclude, though reactions in the different alcohols show different product distributions after 24 h, the overall yield of useful products including the biofuel components and HMF, is comparable. But also, the protective role of the alcohols against HMF conversion into humins is only important when there are considerable amounts of water in the reaction medium. This suggests an active role of water in the polymerization of HMF, as HMF can be fairly stable in the reactive medium in absence of water.

Table 3
Ethanolysis reaction results for different substrates over Si_mC_n-T-SO_3H.[a]

Entry	Substrate	Yields (%)			
		EL	HMF-ethers	α-EGP	β-EGP
1	Fructose	54	9	0	0
2	Inulin	37	6	2	1
3	Sucrose	26	4	16	8
4	Glucose	7	4	33	17
5	Cellulose	1	1	20	10

[a] Reaction conditions: substrate (1 mmol monomeric units), $Si_{50}C_{50}$-400-SO_3H (50 mg), methyl naphthalene (20 mg) as internal standard, ethanol (2.67 g), 160 °C, 24 h.

3.6. Influence of the fructose concentration and substrate type

Use of high fructose concentration is important for the commercial feasibility of the reaction under study. Experiments with different initial fructose concentrations were therefore carried out over $Si_{50}C_{50}$-400-SO_3H in pure ethanol. The results are collected in Table S1. While keeping the catalyst loading constant (Table S1, entries 1, 3 and 6), EL and (E)HMF yields both decreases progressively with the fructose concentration, while the humins formation increased at full fructose conversion. Use of higher fructose concentration thus compromises the selective conversion of fructose. Since the addition of more catalyst is unable to avoid the large humins formation at high fructose concentration (Table S1, entries 2, 4 and 7), the direct role of fructose in humins formation seems limited. Though a concentration effect in (higher order) humins formation may be expected, the role of the additionally formed water for higher concentration reactions may not be underestimated.

The Si_mC_n-T-SO_3H sulfonated composite catalysts were also used for the ethanolysis of other biomass-related substrates. Natural resources of fructose and glucose were tested to produce the chemicals and biofuel components. The results are summarized in Table 3. Inulin conversion in ethanol shows substantial product yields. EL (37%) and EMF (6%) are the dominant products after 24 h, but there is also formation of 3% EGP, which is a likely consequence of the minor glucose units in inulin. The formation of products supports the ability of the mesoporous catalyst to perform solvolysis catalysis, albeit somewhat less efficient to reach the active sites. Sucrose, a non-reducing disaccharide of fructose and glucose, converts already much better. Being a small molecule, the catalytic ethanolysis runs sufficiently fast, producing half equivalent of fructose, which is converted into EL and EMF, and half equivalent of ethyl glucoside isomers (EGPs), which remain stable under reaction conditions. Indeed, glucose conversion leads to the dominant formation of EGP, pointing to the importance of fructose as precursor of EMF and EL. The sulfonated composites clearly are inefficient isomerization catalysts, allowing them to favor the synthesis of EGP isomers in agreement with a very recent publication of Corma et al. [96] The production of EL and EMF from glucose sources (like starch, cellulose) therefore requires an additional isomerization activity, which is usually based on Lewis acid catalysis

[91]. The lack of isomerization though is not common for a sulfonic acid catalyst, since formation of HMF (derivatives) and levulinic acid (ester) from cellulose has been reported in presence of different (supported) sulfonic acids [97]. It is however not clear how to define the active site ('s environment) explaining the isomerization activity. EGPs are also predominantly formed from cellulose. Their high yields corroborate the ability of the mesoporous composites to solvolyze large biopolymers like cellulose, thanks to the high surface area. Hydrolysis of cellulose with highly disperse carbon is a major recent research topic [22,25].

4. Conclusions

An EISA like method using a sucrose-TEOS-F127 system is developed to create novel mesoporous sulfonated silica-carbon nanocomposites with varying carbon content and porosity. Their structure is able to withstand harsh sulfonation conditions, creating a solid sulfonic acid silica-carbon composites, in which the sulfonic acid groups are associated to the carbon phase. The acid property of the composites was studied for the one-pot catalytic conversion of fructose in ethanol. The potential biofuels, EL and HMF-ethers (EMF and DEMEMF) were produced at high combined yields of 70–80% at short reaction times. The catalyst can be stored for a very long time under ambient conditions without compromising the structural and catalytic properties. Though loss of catalytic activity was measured for consecutive runs, the catalytic activity can be fully restored upon re-sulfonating the spent catalyst. Main cause of deactivation is not a loss of active groups into the solution, but rather a fouling of the acid sites and blockage of the pores by humins is suggested. The best catalytic results were obtained with nanocomposites having a high loading of sulfonic acid groups. Since their accessibility in the nanocomposite is crucial, the amount of carbon and the pyrolysis temperature need to be controlled well. A simplified reaction kinetic model is proposed for modeling of the experimental reaction results in presence of the nanocomposites. The mechanism and the role of the acid catalysis show large resemblance with that in presence of H_2SO_4, except that here an additional direct conversion of HMF to EL was required to fit the kinetics. Humins formation can be reduced by working at low temperature, but also by performing the fructose reaction in presence of low water concentration in alcoholic solvents. Though the protective role of the alcohol may be used to explain the higher product yields, it does not explain the high HMF yield obtained in *tert*-butanol. The direct role of water in forming humins from HMF is likely underestimated.

Acknowledgments

R.Z. and Y.L. acknowledge the Chinese Scholarship Council (No. 201206210307 and No. 201404910467 respectively) for financial support. F.Y. acknowledges a DBOF doctoral fellowship from KU Leuven. W.S. acknowledges KU Leuven for a postdoctoral fellowship.

Appendix A. Supplementary data

Supplementary data associated with this article can be found, in the online version, at http://dx.doi.org/10.1016/j.apcatb.2016.12.053.

References

[1] J.H. Clark, F.I. Deswarte, Introduction to Chemicals from Biomass, John Wiley & Sons, 2014.
[2] J.C. Serrano-Ruiz, J.A. Dumesic, Energy Environ. Sci. 4 (2011) 83–99.
[3] A. Corma, S. Iborra, A. Velty, Chem. Rev. 107 (2007) 2411–2502.
[4] M. Dusselier, M. Mascal, B.F. Sels, Top. Curr. Chem. 353 (2014) 1–40.
[5] P. Gallezot, ChemSusChem 1 (2008) 734–737.
[6] J.S. Luterbacher, D. Martin Alonso, J.A. Dumesic, Green Chem. 16 (2014) 4816–4838.
[7] S. Van den Bosch, W. Schutyser, R. Vanholme, T. Driessen, S.F. Koelewijn, T. Renders, B. De Meester, W.J.J. Huijgen, W. Dehaen, C.M. Courtin, B. Lagrain, W. Boerjan, B.F. Sels, Energy Environ. Sci. 8 (2015) 1748–1763.
[8] B. Op De Beeck, M. Dusselier, J. Geboers, J. Holsbeek, E. Morré, S. Oswald, L. Giebeler, B.F. Sels, Energy Environ. Sci. 8 (2015) 230–240.
[9] C.E. Wyman, Aqueous Pretreatment of Plant Biomass for Biological and Chemical Conversion to Fuels and Chemicals, John Wiley & Sons, 2013.
[10] P. Gallezot, Chem. Soc. Rev. 41 (2012) 1538–1558.
[11] P.S. Nigam, A. Singh, Prog. Energy Combust. 37 (2011) 52–68.
[12] O.O. James, S. Maity, L.A. Usman, K.O. Ajanaku, O.O. Ajani, T.O. Siyanbola, S. Sahu, R. Chaubey, Energy Environ. Sci. 3 (2010) 1833.
[13] A. Deneyer, T. Renders, J. Van Aelst, S. Van den Bosch, D. Gabriëls, B.F. Sels, Curr. Opin. Chem. Biol. 29 (2015) 40–48.
[14] P. Ferrini, R. Rinaldi, Angew. Chem. Int. Ed. 53 (2014) 8634–8639.
[15] M.V. Galkin, J.S.M. Samec, ChemSusChem 7 (2014) 2154–2158.
[16] T. Renders, W. Schutyser, S. Van den Bosch, S. Koelewijn, T. Vangeel, C.M. Courtin, B.F. Sels, ACS Catal. 6 (2016) 2055–2066.
[17] W. Schutyser, S. Van den Bosch, T. Renders, T. De Boe, S.F. Koelewijn, A. Dewaele, T. Ennaert, O. Verkinderen, B. Goderis, C.M. Courtin, B.F. Sels, Green Chem. 17 (2015) 5035–5045.
[18] Q. Song, F. Wang, J. Cai, Y. Wang, J. Zhang, W. Yu, J. Xu, Energy Environ. Sci. 6 (2013) 994.
[19] H. Kobayashi, M. Yabushita, T. Komanoya, K. Hara, I. Fujita, A. Fukuoka, ACS Catal. 3 (2013) 581–587.
[20] J. Ni, H. Wang, Y. Chen, Z. She, H. Na, J. Zhu, Bioresour. Technol. 137 (2013) 106–110.
[21] H. Kobayashi, T. Komanoya, K. Hara, A. Fukuoka, ChemSusChem 3 (2010) 440–443.
[22] M. Yabushita, H. Kobayashi, K. Hara, A. Fukuoka, Catal. Sci. Technol. 4 (2014) 2312–2317.
[23] S. Van de Vyver, L. Peng, J. Geboers, H. Schepers, F. de Clippel, C.J. Gommes, B. Goderis, P.A. Jacobs, B.F. Sels, Green Chem. 12 (2010) 1560.
[24] K. Nakajima, M. Hara, ACS Catal. 2 (2012) 1296–1304.
[25] P. Chung, M. Yabushita, A.T. To, Y. Bae, J. Jankolovits, H. Kobayashi, A. Fukuoka, A. Katz, ACS Catal. 5 (2015) 6422–6425.
[26] S. Van de Vyver, J. Geboers, P.A. Jacobs, B.F. Sels, ChemCatChem 3 (2011) 82–94.
[27] J.A. Geboers, S. Van de Vyver, R. Ooms, B. Op De Beeck, P.A. Jacobs, B.F. Sels, Catal. Sci. Technol. 1 (2011) 714.
[28] C. Chatterjee, F. Pong, A. Sen, Green Chem. 17 (2015) 40–71.
[29] W. Deng, Q. Zhang, Y. Wang, Sci. China Chem. 58 (2015) 29–46.
[30] T. Wang, M.W. Nolte, B.H. Shanks, Green Chem. 16 (2014) 548–572.
[31] S. Dutta, S. De, B. Saha, Biomass Bioenergy 55 (2013) 355–369.
[32] D.W. Rackemann, W.O. Doherty, Biofuels. Bioprod. Biorefin. 5 (2011) 198–214.
[33] F. Yu, J. Thomas, M. Smet, W. Dehaen, B.F. Sels, Green Chem. 18 (2016) 1694–1705.
[34] J.J. Pacheco, M.E. Davis, Proc. Natl. Acad. Sci. 111 (2014) 8363–8367.
[35] J. Zhang, S. Wu, B. Li, H. Zhang, ChemCatChem 4 (2012) 1230–1237.
[36] R. van Putten, J.C. van der Waal, E. de Jong, C.B. Rasrendra, H.J. Heeres, J.G. de Vries, Chem. Rev. 113 (2013) 1499–1597.
[37] J.N. Chheda, G.W. Huber, J.A. Dumesic, Angew. Chem. Int. Ed. 46 (2007) 7164–7183.
[38] G.W. Huber, S. Iborra, A. Corma, Chem. Rev. 106 (2006) 4044–4098.
[39] C.M. Lew, N. Rajabbeigi, M. Tsapatsis, Ind. Eng. Chem. Res. 51 (2012) 5364–5366.
[40] L. Bing, Z. Zhang, K. Deng, Ind. Eng. Chem. Res. 51 (2012) 15331–15336.
[41] A.J.J.E. Eerhart, A.P.C. Faaij, M.K. Patel, Energy Environ. Sci. 5 (2012) 6407.
[42] A.J.J.E. Eerhart, M.K. Patel, A.P.C. Faaij, Biofuels. Bioprod. Biorefin. 9 (2015) 307–325.
[43] B. Liu, Z. Zhang, RSC Adv. 3 (2013) 12313.
[44] M. Balakrishnan, E.R. Sacia, A.T. Bell, Green Chem. 14 (2012) 1626.
[45] H. Wang, T. Deng, Y. Wang, X. Cui, Y. Qi, X. Mu, X. Hou, Y. Zhu, Green Chem. 15 (2013) 2379.
[46] P. Russo, M.M. Antunes, P. Neves, P.V. Wiper, E. Fazio, F. Neri, F. Barrreca, L. Mafra, M. Pillinger, N. Pinna, A.A. Valente, Green Chem. (2014) 4292–4305.
[47] P. Lanzafame, D.M. Temi, S. Perathoner, G. Centi, A. Macario, A. Aloise, G. Giordano, Catal. Today 175 (2011) 435–441.
[48] P. Lanzafame, K. Barbera, S. Perathoner, G. Centi, A. Aloise, M. Migliori, A. Macario, J.B. Nagy, G. Giordano, J. Catal. 330 (2015) 558–568.
[49] K. Barbera, P. Lanzafame, A. Pistone, S. Millesi, G. Malandrino, A. Gulino, S. Perathoner, G. Centi, J. Catal. 323 (2015) 19–32.
[50] P. Che, F. Lu, J. Zhang, Y. Huang, X. Nie, J. Gao, J. Xu, Bioresour. Technol. 119 (2012) 433–436.
[51] M. Mascal, E.B. Nikitin, Angew. Chem. Int. Ed. 47 (2008) 7924–7926.
[52] G.A. Kraus, T. Guney, Green Chem. 14 (2012) 1593–1596.
[53] A. Liu, Z. Zhang, Z. Fang, B. Liu, K. Huang, J. Ind. Eng. Chem. 20 (2014) 1977–1984.
[54] Z. Yuan, Z. Zhang, J. Zheng, J. Lin, Fuel 150 (2015) 236–242.
[55] H. Li, S. Saravanamurugan, S. Yang, A. Riisager, Green Chem. 18 (2016) 726–734.
[56] Y. Yang, C. Hu, M.M. Abu-Omar, Bioresour. Technol. 116 (2012) 190–194.

[57] J.A. Melero, G. Morales, J. Iglesias, M. Paniagua, B. Hernández, S. Penedo, Appl. Catal. A 466 (2013) 116–122.
[58] M.M. Antunes, P.A. Russo, P.V. Wiper, J.M. Veiga, M. Pillinger, L. Mafra, D.V. Evtuguin, N. Pinna, A.A. Valente, ChemSusChem 7 (2014) 804–812.
[59] M. Mascal, E.B. Nikitin, Green Chem. 12 (2010) 370.
[60] G.M. Gonzalez Maldonado, R.S. Assary, J.A. Dumesic, L.A. Curtiss, Energy Environ. Sci. 5 (2012) 8990–8997.
[61] S. Saravanamurugan, A. Riisager, Catal. Commun. 17 (2012) 71–75.
[62] L. Peng, L. Lin, H. Li, Q. Yang, Appl. Energy 88 (2011) 4590–4596.
[63] R. Liu, J. Chen, X. Huang, L. Chen, L. Ma, X. Li, Green Chem. 15 (2013) 2895–2903.
[64] E.C. Njagi, H.C. Genuino, C. Kuo, S. Dharmarathna, A. Gudz, S.L. Suib, Micropor. Mesopor. Mater. 202 (2015) 68–72.
[65] L. Peng, L. Lin, J. Zhang, J. Shi, S. Liu, Appl. Catal. A 397 (2011) 259–265.
[66] S. Saravanamurugan, A. Riisager, ChemCatChem 5 (2013) 1754–1757.
[67] D. Ding, J. Xi, J. Wang, X. Liu, G. Lu, Y. Wang, Green Chem. 17 (2015) 4037–4044.
[68] J. Wang, W. Xu, J. Ren, X. Liu, G. Lu, Y. Wang, Green Chem. 13 (2011) 2678.
[69] F.H. Richter, K. Pupovac, R. Palkovits, F. Schüth, ACS Catal. 3 (2013) 123–127.
[70] X. Mo, E. Lotero, C. Lu, Y. Liu, J.G. Goodwin, Catal. Lett. 123 (2008) 1–6.
[71] L. Peng, A. Philippaerts, X. Ke, J. Van Noyen, F. De Clippel, G. Van Tendeloo, P.A. Jacobs, B.F. Sels, Catal. Today 150 (2010) 140–146.
[72] W. Lou, Q. Guo, W. Chen, M. Zong, H. Wu, T.J. Smith, ChemSusChem 5 (2012) 1533–1541.
[73] B. Chang, J. Fu, Y. Tian, X. Dong, RSC Adv. 3 (2013) 1987–1994.
[74] R. Xing, N. Liu, Y. Liu, H. Wu, Y. Jiang, L. Chen, M. He, P. Wu, Adv. Funct. Mater. 17 (2007) 2455–2461.
[75] L. Wang, J. Zhang, S. Yang, Q. Sun, L. Zhu, Q. Wu, H. Zhang, X. Meng, F. Xiao, J. Mater. Chem. A 1 (2013) 9422.
[76] D. Nandan, P. Sreenivasulu, L.N. Sivakumar Konathala, M. Kumar, N. Viswanadham, Micropor. Mesopor. Mater. 179 (2013) 182–190.
[77] M. Okamura, A. Takagaki, M. Toda, J.N. Kondo, K. Domen, T. Tatsumi, M. Hara, S. Hayashi, Chem. Mater. 18 (2006) 3039–3045.
[78] A.J. Crisci, M.H. Tucker, M. Lee, S.G. Jang, J.A. Dumesic, S.L. Scott, ACS Catal. 1 (2011) 719–728.
[79] P. Valle-Vigón, M. Sevilla, A.B. Fuertes, Appl. Surf. Sci. 261 (2012) 574–583.
[80] N. Pal, A. Bhaumik, Adv. Colloid Interface 189–190 (2013) 21–41.
[81] F. de Clippel, M. Dusselier, S. Van de Vyver, L. Peng, P.A. Jacobs, B.F. Sels, Green Chem. 15 (2013) 1398.
[82] R. Liu, Y. Shi, Y. Wan, Y. Meng, F. Zhang, D. Gu, Z. Chen, B. Tu, D. Zhao, J. Am. Chem. Soc. 128 (2006) 11652–11662.
[83] R. Zhong, L. Peng, F. de Clippel, C. Gommes, B. Goderis, X. Ke, G. Van Tendeloo, P.A. Jacobs, B.F. Sels, ChemCatChem 7 (2015) 3047–3058.
[84] H.N. Pham, A.E. Anderson, R.L. Johnson, K. Schmidt-Rohr, A.K. Datye, Angew. Chem. Int. Ed. 51 (2012) 13163–13167.
[85] R. Zhong, L. Peng, R.I. Iacobescu, Y. Pontikes, R. Shu, L. Ma, B.F. Sels, ChemCatChem (2016), http://dx.doi.org/10.1002/cctc.201600939.
[86] K. Nakajima, M. Okamura, J.N. Kondo, K. Domen, T. Tatsumi, S. Hayashi, M. Hara, Chem. Mater. 21 (2009) 186–193.
[87] F.S. Asghari, H. Yoshida, Ind. Eng. Chem. Res. 46 (2007) 7703–7710.
[88] B.A. Fachri, R.M. Abdilla, H.H.V.D. Bovenkamp, C.B. Rasrendra, H.J. Heeres, ACS Sustain. Chem. Eng. 3 (2015) 3024–3034.
[89] A.M. van der Heijden, F. van Rantwijk, H. van Bekkum, J. Carbohydr. Chem. 18 (1999) 131–147.
[90] I.A. Ignatyev, P.G.N. Mertens, C. Van Doorslaer, K. Binnemans, D.E. de Vos, Green Chem. 12 (2010) 179–1795.
[91] W.R. Gunther, Y. Wang, Y. Ji, V.K. Michaelis, S.T. Hunt, R.G. Griffin, Y. Roman-Leshkov, Nat. Commun. 3 (2012) 1109.
[92] J. Tan, Q. Liu, C. Cai, S. Qiu, T. Wang, Q. Zhang, L. Ma, G. Chen, RSC Adv. 5 (2015) 58784–58789.
[93] M. Yabushita, H. Kobayashi, J. Hasegawa, K. Hara, A. Fukuoka, ChemSusChem 7 (2014) 1443–1450.
[94] M. Bicker, D. Kaiser, L. Ott, H. Vogel, J. Supercrit. Fluids 36 (2005) 118–126.
[95] X. Hu, C. Li, Green Chem. 13 (2011) 1676–1679.
[96] M.J. Climent, A. Corma, S. Iborra, S. Martínez-Silvestre, ChemSusChem (2016), http://dx.doi.org/10.1002/cssc.20160097.
[97] F. Yu, R. Zhong, H. Chong, M. Smet, W. Dehaen, B.F. Sels, Green Chem. (2016), http://dx.doi.org/10.1039/C6GC02130A.